Steady shock waves in porous metals: Viscosity and micro-inertia effects

Christophe Czarnota, Alain Molinari, Sébastien Mercier

Steady shock waves in porous metals: viscosity and micro-inertia effects

Christophe Czarnota[a,*], Alain Molinari[a], Sébastien Mercier[a]

[a] *Laboratoire d'Etude des Microstructures et de Mécanique des Matériaux, LEM3 - UMR CNRS 7239, Université de Lorraine - Ile du Saulcy - 57045 METZ Cedex 1 - FRANCE*

Abstract

The structure of steady shock waves in porous solids is a complex phenomenon involving in general the interplay of micro-inertia effects with the nonlinear elastic viscoplastic matrix response. Micro-inertia effects are due to the important acceleration of material particles in the vicinity of collapsing voids. By adopting the analytical approach recently developed for porous metals by Czarnota et al. [J. Mech. Phys. Solids **107** (2017)], we analyze the effects of matrix rate sensitivity, shock stress amplitude and micro-inertia on the structure of planar shock waves. We also analyze the relationship that links the strain rate within the shock to the jump of the stress across the shock. The fourth power law experimentally revealed for dense metals, Swegle & Grady [J. Appl. Phys. **58** (1985)] does not hold for heterogeneous materials. By considering the case of porous aluminum, we show that this relationship is characterized by two distinct regimes: (i) the first regime holds for weak shock intensities and is representative of the viscoplastic response of the dense matrix material, (ii) the second regime, that holds for shock of higher amplitude, is dominated by micro-inertia effects and is strongly influenced by the pore size. Micro-inertia effects appear to be quite beneficial since they are conducive to shock mitigation by attenuating the level of strain rate and of acceleration sustained by material particles.

Keywords: shock waves (A), porous material (B), rate-dependent material (B),

*Corresponding author
Email addresses: christophe.czarnota@univ-lorraine.fr (Christophe Czarnota), alain.molinari@univ-lorraine.fr (Alain Molinari), sebastien.mercier@univ-lorraine.fr (Sébastien Mercier)

Nomenclature

$a_0,\ a$	initial and current void radii
$a_1, ...,\ a_6$	elastic constants
$C,\ C^{\mathrm{e}}$	plastic and elastic shockwave speeds
$c_L,\ c_S$	longitudinal and shear wave speeds in the matrix
c_1	rate dependent property of the matrix
$\mathbf{D}^{\mathrm{p}}$	plastic strain rate tensor
E_{eq}	accumulated plastic strain
$\mathbf{F},\ \mathbf{F}^{\mathrm{e}},\ \mathbf{F}^{\mathrm{p}}$	total, elastic and plastic deformation gradient tensors
$F_1(\varepsilon_1^{\mathrm{e}}, \varepsilon_2^{\mathrm{e}}),\ F_2(\varepsilon_1^{\mathrm{e}}, \varepsilon_2^{\mathrm{e}})$	functions related to elastic strains
$f_0,\ f$	initial and current porosities
$H,\ h^{\mathrm{p}}$	parameters of the Swegle and Grady relationship for porous material
$h_{\mathrm{MR}},\ h^{\mathrm{p}}_{\mathrm{MR}}$	exponents of two relationships obtained by Molinari & Ravichandran (2004) for dense aluminum
m	strain rate sensitivity
$M = 1/m$	inverse of the strain rate sensitivity
n	strain hardening parameter
t	time
$T_1^\star$	rate dependent property of the matrix
$\mathbf{T}$	first Piola-Kirchhoff stress tensor
$v,\ v^{\mathrm{e}}$	particle velocity respectively in the plastic and in the elastic shocks
X, x	longitudinal position in the initial and current configurations
γ_0	reference strain
γ^{p}	plastic shear strain
$\dot{\kappa}$	plastic multiplier
$\lambda_1,\ \lambda_1^{\mathrm{e}},\ \lambda_1^{\mathrm{p}}$	total, elastic and plastic axial stretches

$\lambda_2,\ \lambda_2^{\mathrm{e}},\ \lambda_2^{\mathrm{p}}$	total, elastic and plastic transverse stretches
σ	compressive stress (positive in compression)
σ_{a0}	matrix stress at zero plastic strain
$\bar{\sigma}$	average effective stress in the matrix
$\bar{\sigma}_a$	rate independent yield strength in the matrix
$\mathbf{\Sigma},\ \mathbf{\Sigma}^\star,\ \mathbf{\Sigma}^{\mathrm{dyn}}$	total, static and dynamic Cauchy stress tensors
$\Omega(\mathbf{\Sigma}^\star, \bar{\sigma}, f)$	viscoplastic flow surface
$\Omega_a(\mathbf{\Sigma}, \bar{\sigma}_a, f)$	rate independent flow surface
Φ	plastic shear strain rate
$\xi = X - Ct$	moving coordinate
$\rho_{0\mathrm{m}}$	matrix mass density
$(\bullet)',\ (\bullet)_{\mathrm{m}},\ (\bullet)_{\mathrm{eq}}$	deviatoric, mean and equivalent parts of the second order tensor $(\bullet)$
$(\bullet)^+,\ (\bullet)^-,\ (\bullet)^{\mathrm{e}}$	variable $(\bullet)$ defined at states (+), (-) and (e)

1. Introduction

The analysis of plastic shock waves in ductile metallic materials has received a lot of attention in military and civilian applications, e.g. Nesterenko (2001); Kitagawa et al. (2009). In particular, it is of crucial importance for security purposes to find ways of reducing the severity of a shock wave by an appropriate design of the rheology and of the internal architecture of materials used for protective devices, e.g. to prevent in-structure electronic components or human bodies from excessive acceleration forces. In some simplified approaches material responses are considered as being rate independent. Then, shocks are modeled as moving surfaces of discontinuities, across which some physical parameters are subjected to an instantaneous jump. However, for real materials, dissipative effects inherited from the material rate dependence and dispersive effects due to material heterogeneities provide a smooth (albeit rapid) variation of physical parameters across a thin shock layer. Shock structure is therefore complex in nature and the wave profile, e.g. generated from an instantaneous change in velocity during impact, generally evolves as a dual structure with an elastic shock followed by a smooth transition (plastic shock) up to the final wave amplitude. Basically, a shock

wave is formed due to steepening effects as a consequence of the nonlinear compressibility of the material and tends to be steady (beyond a certain propagation distance from the impacted plane) when these effects are balanced by dissipative and dispersive mechanisms mentioned above.

The aim of this paper is to analyze the structure of steady plastic shock waves in porous metals. Transient regime, elastic precursor and wave attenuation that can be investigated by finite element modeling, fall out of the scope of the paper where a fully analytical approach is adopted. Advantages of steady wave approaches is that a detailed description of the steady shock structure (and associated material state) is obtained at very low computational cost when compared to finite element calculations, Lloyd et al. (2015). In addition, some explicit relationships can be derived that allow to shed light on the effects of material and loading parameters. With the possibility of designing the internal architecture of a porous material with additive manufacturing, a wide range of applications is open in terms of optimal material design for security purposes. Therefore, it is appealing to develop a fundamental analysis of the relationship between material characteristics (i.e. rheological properties and internal architecture) and plastic shock structure. We consider here a simple internal configuration: a population of spherical voids, with same initial radius, isotropically distributed inside a viscoplastic metallic matrix. Thus, the internal configuration of the material is solely described by two parameters: the initial porosity f_0 and the initial void radius a_0. Consequently, the shock structure should be a priori affected by f_0, a_0 and by the matrix rate dependence.

However, it appears of fundamental importance to consider an additional aspect. A rapid void-collapse is induced by the plastic shock wave which leads to an intense local acceleration of material particles in the vicinity of micro-voids. From Newton's second law, inertia forces are generated at the microscale. The overall response of porous metals can be strongly affected by these micro-inertia effects which become significant when high strain rates are considered.

The pioneering work of Carroll & Holt (1972) on dynamic pore collapse of ductile materials containing spherical voids has inspired many researchers who developed analytical studies based on a similar formalism (hollow sphere model or spherical void

embedded in an infinite matrix under remote dynamic spherical compressive or tensile loading). The micro-inertia contribution introduced by Carroll & Holt (1972) was then combined to the effect of material viscosity, strain hardening and thermal softening, e.g. see Johnson (1981); Carroll et al. (1986); Ortiz & Molinari (1992); Cortés (1992); Tong & Ravichandran (1993, 1995); Wu et al. (2003a,b,c); Wilkerson & Ramesh (2014); Wilkerson (2017). Various constitutive laws have been considered in the literature (different materials or different formulations of the matrix viscoplasticity) but trends and main results remain the same. For a power-law type viscoplasticity model, Ortiz & Molinari (1992) showed that viscous effects are dominant at the early stage of the spherical void growth while micro-inertia is particularly significant when voids reach a critical size. Making use of the dislocation-based viscoplasticity model of Austin & McDowell (2011), Wilkerson & Ramesh (2014) gave an estimate of the void transition size based on the steady state growth rate previously derived by Molinari & Wright (2005). The combined influence of micro-inertia and viscous effects has also been analyzed and inertia was shown to govern the dynamics of large voids with large mobile dislocation densities, while dislocation dynamics dominates for small voids and lower mobile dislocation densities. More importantly, Wilkerson & Ramesh (2014) confirmed the need to account for both of these phenomena, see also Wilkerson (2017) for an extension.

Another direction of the theoretical works is associated with dynamic homogenization approaches based on the principle of virtual power, Wang (1994, 1997); Molinari & Mercier (2001). Molinari & Mercier (2001) considered the hollow sphere model and the trial velocity field of Gurson (1977) to derive an explicit constitutive behavior for general states of stress, accounting for micro-inertia and viscoplasticity. Previous trends were confirmed on the role played by viscous and micro-inertia effects. The modeling of Molinari & Mercier (2001) has been used in Czarnota et al. (2006, 2008); Jacques et al. (2010); Versino & Bronkhorst (2018) to describe spall fracture due to micro-voiding in a high purity grade tantalum, or in Czarnota et al. (2017) and Barthélémy et al. (2016); Jacques & Barthélémy (2018) for shock wave propagation in porous materials and foams respectively.

The interplay between inertial and viscous effects has been examined in the time

dependence of pore collapse and both effects are shown to delay the densification of porous materials. Butcher et al. (1974) incorporated the effect of the deviatoric stress in the original model of Carroll & Holt (1972) and a term representing material viscosity was added to the hydrostatic stress (linear viscous rate dependence). The authors concluded that the material viscosity rather than the material inertia is the dominant parameter controlling the void closure. This trend is attributed to the strong rate dependence brought by Newtonian viscosity. By contrast, when considering a power law viscoplastic matrix material, Tong & Ravichandran (1993) highlighted that micro-inertia is strongly influencing the dynamic response when the initial void size is large enough. Note also that dynamic compaction of aluminum nanopowders has been recently studied from molecular dynamics in the work of Krasnikov & Mayer (2015), Xiang et al. (2017) and Mayer et al. (2020). The later work stressed that micro-inertia is responsible for the deviation from the quasistatic response.

The plastic shock layer width is a particular characteristic reflecting the severity of a shock wave. It was investigated by Dunin & Surkov (1979) using the hollow sphere model. The micro-inertia contribution (based on the approach of Carroll & Holt, 1972) was included and the influence of viscous effects was accounted for through a newtonian type law. When viscosity was neglected, the shock layer width was found to be determined mainly by the geometry of the void irrespective of the magnitude of the shock pressure. This may be the consequence of the influence of the void radius on micro-inertia effects. More recently, Czarnota et al. (2017) developed a micro-inertia dependent model founded on the dynamic homogenization procedure of Molinari & Mercier (2001). In this work, the matrix behavior was defined using the constitutive law of Clifton (1970) for aluminum. For a given shock stress amplitude, the authors showed that the shock layer width in porous aluminum may be larger than in dense aluminum if the initial pore size is large enough. Furthermore, when micro-inertia overwhelms viscous rate effect, the shock layer width was found to be scaled by the initial void radius (see also Carroll et al., 1986, for an alternative scaling law also involving the void size).

In fact, in addition to be scaled by the matrix mass density and influenced by the void size (and void aspect ratio if spheroidal or cylindrical voids are considered, see

Sartori et al., 2015; Subramani et al., 2020) micro-inertia effects contain a specific rate influence, Molinari & Mercier (2001). As a consequence, two rate sensitivities of different natures are brought into the problem: (i) firstly we have to consider the intrinsic rate sensitivity related to the viscoplastic response of the metal matrix, (ii) secondly, an additional rate dependence, due to micro-inertia effects, has to be accounted for. How the shock layer is modulated by the internal structure of the material (parameters f_0 and a_0) and the rate dependencies of different physical natures (matrix response and microscale inertia) is the subject of the present investigation. In addition, the shock intensity has an important effect. The relative effects of matrix rate dependence and micro-inertia in terms of shock intensity will be elucidated. In that perspective, we take porous aluminum as a reference material and, for the purpose of a parametric analysis, we consider a class of model materials obtained by varying the matrix rate sensitivity.

Shocks of relatively small intensity are considered so that temperature effects can be neglected. In addition, for moderate shock intensities the collapse mechanism is supposed to be controlled by plastic deformation of the matrix material without any instability phenomenon such as jet formation at the void surface (see Xiang et al., 2017, for an illustration by molecular dynamics simulations, of the collapse process from plasticity driven to internal jetting).

Sections 2 presents the kinematics of the planar impact test and recall the constitutive relationships for porous materials developed in Czarnota et al. (2017). The modeling is valid for uniaxial strain condition which corresponds to the framework analyzed in the present work. Section 3 begins with a presentation of the quasistatic compression curve which is used in place of the Hugoniot for the analysis of shocks of moderate amplitudes. Then, an approximate analytical solution of the relationship between the plastic shock speed and the particle velocity is addressed. Its derivation is detailed in Appendix A. Section 4 illustrates the interplay of viscous and micro-inertia effects on shock structure and shock layer width. Viscous and micro-inertia dominated regimes are respectively brought into light and the transition between these regimes is analyzed in terms of void radius and loading rate effects. For an intermediate range of shock pressures, the shock layer is found structured by the combined effects of matrix

rate sensitivity and microscale inertia. In section 5, it is found that a single power law (Swegle and Grady law) cannot be used to characterize the level of strain rate within the shock in terms of the shock stress. Rather, two distinct power laws are defined for respectively the viscous dominated regime (low shock stress) and the micro-inertia dominated regime (large shock stress).

2. Kinematics and constitutive relationships

2.1. Kinematics

Consider a planar impact experiment on a porous isotropic sample with initial porosity f_0 and current porosity f. Upon impact, two waves are usually generated i.e. an elastic precursor followed by a plastic shock wave. Under certain circumstances, a plastic fan (along which material particles face a gradual change in the wave speed as the stress is increasing) connecting the elastic shock to the plastic shock can also be observed, Knowles (2002); Czarnota et al. (2017). For large shock amplitudes, steady plastic shocks are established beyond a certain propagation distance from the impacted plane. In this case, the plastic shock propagates with a constant shape and a constant speed., see Fig. 1. For the analytical description of shock structures in porous metals we adopt the modeling of Czarnota et al. (2017), valid for uniaxial strain condition.

The kinematic is that of uniaxial deformation with compressive loading (void collapse). The problem is expressed in the Lagrangian formalism. The orthonormal frame basis $(\mathbf{e}_1,\ \mathbf{e}_2,\ \mathbf{e}_3)$ is introduced with $\mathbf{e}_1$ aligned with the wave propagation direction. We denote by X (respectively x) the longitudinal position of a material particle in the initial (respectively current) configuration. The longitudinal displacement of a material particle is $u = x - X$, the longitudinal stretch is $\lambda_1 = \frac{\partial x}{\partial X} = 1 + \frac{\partial u}{\partial X}$ and the deformation gradient tensor $\mathbf{F}$ is expressed in the orthonormal frame basis $(\mathbf{e}_1,\ \mathbf{e}_2,\ \mathbf{e}_3)$ as:

$$\mathbf{F} = \lambda_1 \mathbf{e}_1 \otimes \mathbf{e}_1 + \mathbf{e}_2 \otimes \mathbf{e}_2 + \mathbf{e}_3 \otimes \mathbf{e}_3 \tag{1}$$

where $\otimes$ stands for the tensor product. Using the standard multiplicative decomposition $\mathbf{F} = \mathbf{F}^{\mathrm{e}}\mathbf{F}^{\mathrm{p}}$, the deformation gradient can be decomposed into elastic and plastic parts,

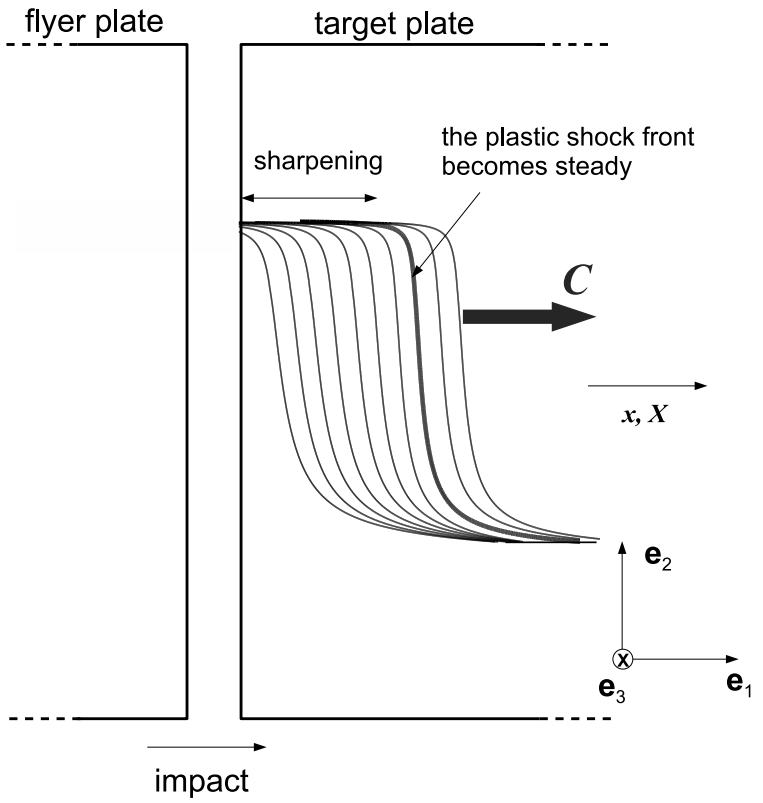

Figure 1: Planar impact experiment of a homogeneous equivalent medium representative of a porous solid. The loading direction is $\mathbf{e_1}$. Under large enough loading amplitude, and if the impacted sample is sufficiently thick, a stationary plastic shock forms beyond a certain propagation distance. The steady shock front propagates with a constant shape, at a constant speed C. The elastic precursor is not represented in this diagram.

where

$$\mathbf{F}^{\mathrm{e}} = \lambda_1^{\mathrm{e}} \mathbf{e}_1 \otimes \mathbf{e}_1 + \lambda_2^{\mathrm{e}} (\mathbf{e}_2 \otimes \mathbf{e}_2 + \mathbf{e}_3 \otimes \mathbf{e}_3) \,, \tag{2}$$

$$\mathbf{F}^{\mathrm{p}} = \lambda_1^{\mathrm{p}} \mathbf{e}_1 \otimes \mathbf{e}_1 + \lambda_2^{\mathrm{p}} (\mathbf{e}_2 \otimes \mathbf{e}_2 + \mathbf{e}_3 \otimes \mathbf{e}_3) \,. \tag{3}$$

λ_i^{e} (respectively λ_i^{p}), $i = 1, 2$, stand for elastic (respectively plastic) stretches along the direction e_i. The porosity evolution during elastic loading is assumed negligible so that f coincides with the porosity in the intermediate configuration. Considering in addition that the matrix is plastically incompressible, one obtains (see Czarnota et al., 2017, for more details):

$$\lambda_1^{\mathrm{e}} = \frac{\lambda_1}{\lambda_1^{\mathrm{p}}} \,, \lambda_2^{\mathrm{e}} = \left(\frac{1 - f_0}{1 - f} \right)^{-1/2} \left(\lambda_1^{\mathrm{p}} \right)^{1/2} \,, \lambda_2^{\mathrm{p}} = \left(\frac{1 - f_0}{1 - f} \right)^{1/2} \left(\lambda_1^{\mathrm{p}} \right)^{-1/2} \,. \tag{4}$$

From Eqs (3-4), the macroscopic plastic strain rate $\mathbf{D}^{\mathrm{p}} = \dot{\mathbf{F}}^{\mathrm{p}} (\mathbf{F}^{\mathrm{p}})^{-1}$ is expressed as:

$$\mathbf{D}^{\mathrm{p}} = \frac{\dot{\lambda}_1^{\mathrm{p}}}{\lambda_1^{\mathrm{p}}} \mathbf{e}_1 \otimes \mathbf{e}_1 - \frac{1}{2} \left(\frac{\dot{\lambda}_1^{\mathrm{p}}}{\lambda_1^{\mathrm{p}}} - \frac{\dot{f}}{1 - f} \right) (\mathbf{e}_2 \otimes \mathbf{e}_2 + \mathbf{e}_3 \otimes \mathbf{e}_3) \,, \tag{5}$$

where the overdot stands for the time derivative operator. From Eq. (5), the mean plastic strain rate $D_{\mathrm{m}}^{\mathrm{p}} = \dfrac{1}{3} \mathrm{tr}(\mathbf{D}^{\mathrm{p}})$ (tr standing for the trace operator) is :

$$D_{\mathrm{m}}^{\mathrm{p}} = \frac{\dot{f}}{3(1 - f)} \,, \tag{6}$$

and the equivalent plastic strain rate $D_{\mathrm{eq}}^{\mathrm{p}} = \sqrt{\dfrac{2}{3} \mathbf{D}^{\mathrm{p}'} : \mathbf{D}^{\mathrm{p}'}}$, $\mathbf{D}^{\mathrm{p}'}$ being the deviatoric part of $\mathbf{D}^{\mathrm{p}}$, is given by:

$$D_{\mathrm{eq}}^{\mathrm{p}} = D_{\mathrm{m}}^{\mathrm{p}} - \frac{\dot{\lambda}_1^{\mathrm{p}}}{\lambda_1^{\mathrm{p}}} \,. \tag{7}$$

The accumulated plastic strain is defined as:

$$E_{\mathrm{eq}}^{\mathrm{p}} = \int_0^t D_{\mathrm{eq}}^{\mathrm{p}}(t') dt' \,. \tag{8}$$

2.2. Constitutive equations

The analysis is restricted to moderate shocks. Thus, temperature effects are neglected and the equation of conservation of energy is not used in the problem. The kinematic compatibility equation is given by:

$$\frac{\partial v}{\partial X} = \frac{\partial \lambda_1}{\partial t} . \tag{9}$$

where t is time, $v = \frac{\partial u}{\partial t}$ is the particle velocity. The Lagrangian form of the conservation of linear momentum is written as:

$$\frac{\partial T_1}{\partial X} = \rho_{0\mathrm{m}}(1 - f_0)\frac{\partial v}{\partial t}, \tag{10}$$

where $\rho_{0\mathrm{m}}$ is the matrix mass density in the reference configuration and T_1 is the component of the first Piola Kirchhoff stress tensor in the wave propagation direction. Because of axisymmetry, the first Piola Kirchhoff stress tensor has the form:

$$\mathbf{T} = T_1 \mathbf{e}_1 \otimes \mathbf{e}_1 + T_2(\mathbf{e}_2 \otimes \mathbf{e}_2 + \mathbf{e}_3 \otimes \mathbf{e}_3)\,, \tag{11}$$

and the Cauchy stress tensor $\mathbf{\Sigma}$, related to $\mathbf{T}$ through $\mathbf{T} = \det(\mathbf{F})\mathbf{\Sigma}\mathbf{F}^{-\mathbf{T}}$, is written as follows:

$$\mathbf{\Sigma} = T_1 \mathbf{e}_1 \otimes \mathbf{e}_1 + \frac{T_2}{\lambda_1}(\mathbf{e}_2 \otimes \mathbf{e}_2 + \mathbf{e}_3 \otimes \mathbf{e}_3)\,. \tag{12}$$

T_2 defines the stress components in the direction orthogonal to the wave propagation direction.

2.2.1. Nonlinear elasticity

Nonlinear elasticity is integrated in the modeling by modifying the internal strain energy proposed by Clifton (1970) for dense aluminum, in order to account for the effect of porosity, Czarnota et al. (2017). The first Piola Kirchhoff stress tensor components of the porous medium are expressed as:

$$T_1 = \frac{\rho_{0\mathrm{m}}(1 - f_0)}{\lambda_1^{\mathrm{p}}} G(f) F_1\left(\varepsilon_1^{\mathrm{e}}, \varepsilon_2^{\mathrm{e}}\right), \tag{13a}$$

$$T_2 = \rho_{0\mathrm{m}}\left[(1 - f_0)(1 - f)\lambda_1^{\mathrm{p}}\right]^{1/2} G(f) F_2\left(\varepsilon_1^{\mathrm{e}}, \varepsilon_2^{\mathrm{e}}\right), \tag{13b}$$

where $\varepsilon_1^{\mathrm{e}}$ and $\varepsilon_2^{\mathrm{e}}$ are the elastic deformation components (Biot tensor of elastic deformations):

$$\varepsilon_1^{\mathrm{e}} = \lambda_1^{\mathrm{e}} - 1 = \frac{\lambda_1}{\lambda_1^{\mathrm{p}}} - 1, \tag{14a}$$

$$\varepsilon_2^{\mathrm{e}} = \lambda_2^{\mathrm{e}} - 1 = \left(\frac{1 - f_0}{1 - f}\right)^{-1/2} \left(\lambda_1^{\mathrm{p}}\right)^{1/2} - 1. \tag{14b}$$

The term $G(f)$ in Eq. (13) describes the influence of f on the elastic response. Following Czarnota et al. (2017), we assume that $G(f) = 1 - f$. Derivation of Eqs (13) and

(14) are provided in Supplementary Material of Czarnota et al. (2017). The functions $F_i\left(\varepsilon_1^{\mathrm{e}}, \varepsilon_2^{\mathrm{e}}\right), (i=1,2)$ are solely related to elastic strains:

$$F_i\left(\varepsilon_1^{\mathrm{e}}, \varepsilon_2^{\mathrm{e}}\right) = A_{i1}\varepsilon_1^{\mathrm{e}} + A_{i2}\left(\varepsilon_1^{\mathrm{e}}\right)^2 + B_{i1}\varepsilon_2^{\mathrm{e}} + B_{i2}\left(\varepsilon_2^{\mathrm{e}}\right)^2 + D_i\varepsilon_1^{\mathrm{e}}\varepsilon_2^{\mathrm{e}}\,, \tag{15}$$

with

$$\begin{aligned} A_{11} &= 2a_2\,, \quad A_{12} = 3a_4\,, \\ B_{11} &= 4a_2 + 2a_3\,, \quad B_{12} = 12a_4 + 5a_5 + a_6\,, \\ D_1 &= 12a_4 + 4a_5\,, \end{aligned} \tag{16}$$

$$\begin{aligned} A_{21} &= 2a_2 + a_3\,, \quad A_{22} = 3a_4 + a_5\,, \\ B_{21} &= 4a_2 + a_3\,, \quad B_{22} = 12a_4 + 3a_5\,, \\ D_2 &= 12a_4 + 5a_5 + a_6\,. \end{aligned}$$

Second and third-order elastic constants a_i are involved in $F_i\left(\varepsilon_1^{\mathrm{e}}, \varepsilon_2^{\mathrm{e}}\right), (i=1,2)$. They have been characterized by ultrasonic measurements to describe the nonlinear elastic response of dense aluminum, see Clifton (1970) and Table 1.

Combining Eqs (13a-14), the stress component T_1 can be expressed in terms of λ_1, λ_1^{p} and f:

$$T_1 = T_1(\lambda_1, \lambda_1^{\mathrm{p}}, f)\,. \tag{17}$$

The compressive stress is defined as follows:

$$\sigma = -T_1 > 0\,. \tag{18}$$

2.2.2. Micro-inertia

Under dynamic loading, material particles located near void boundaries undergo large accelerations developed at the microscale. These micro-inertia effects are accounted for based on the dynamic homogenized approach proposed by Molinari & Mercier (2001). In this paper, the macroscopic Cauchy stress tensor $\boldsymbol{\Sigma}$ is shown to be the sum of two contributions:

$$\boldsymbol{\Sigma} = \boldsymbol{\Sigma}^{\star} + \boldsymbol{\Sigma}^{\mathrm{dyn}}. \tag{19}$$

Table 1: Material parameters for 6061-T6 aluminum at room temperature (25°C) and atmospheric pressure (from Molinari & Ravichandran, 2004, and adapted from Clifton, 1970).

$\rho_{0\mathrm{m}} = 2703\mathrm{kg/m}^3$	(mass density)
$c_L = 6368\mathrm{m/s}$	(longitudinal wave speed)
$c_S = 3197\mathrm{m/s}$	(shear wave speed)
First and second order thermoelastic constants (characterized by Clifton (1970) from ultrasonic measurements)	
$a_2 = c_L^2/2 = 20.28 \times 10^6(\mathrm{m/s})^2$; $a_3 = -2c_S^2 = -20.44 \times 10^6(\mathrm{m/s})^2$; $a_4 = -66.4 \times 10^6(\mathrm{m/s})^2$	
$a_5 = 157.5 \times 10^6(\mathrm{m/s})^2$; $a_6 = -142.8 \times 10^6(\mathrm{m/s})^2$	
Rate independent plasticity characteristics, see Eq.(29)	
$\sigma_{a0} = 240\mathrm{MPa}$	(stress at zero plastic strain)
$\gamma_0 = 0.52$	(reference strain)
$n = 1.55$	(hardening parameter)
Rate dependent properties, see Eq. (27)	
$M = 1/m = 1.78$	(inverse of the strain rate sensitivity)
$T_1^\star = 1.6\mathrm{MPa}$	
$K_1 = 393\mathrm{s}^{-1}$	
$K_2 = 149.6$	

$\boldsymbol{\Sigma}^{\text{dyn}}$ is accounting for micro-inertia effects and $\boldsymbol{\Sigma}^{\star}$ is the quasistatic stress that can be obtained from the viscoplastic potential (or flow surface) of the porous material. When micro-inertia effects are disregarded, $\boldsymbol{\Sigma}^{\text{dyn}} = \mathbf{0}$ and $\boldsymbol{\Sigma} = \boldsymbol{\Sigma}^{\star}$.

The dynamic contribution $\boldsymbol{\Sigma}^{\text{dyn}}$ is derived from the general framework developed in Molinari & Mercier (2001). Here, it is assumed that voids are keeping their spherical shape during the deformation process and that the dynamic stress is essentially spherical. Such an approach can be considered for large stress triaxility states as it is the case for planar impacts (see also Czarnota et al., 2006, 2008; Jacques et al., 2010, for applications related to spall fracture). Under such consideration, only the mean stress is affected by micro-inertia and Eq. (19) is expressed as:

$$\Sigma_{\text{m}} = \Sigma_{\text{m}}^{\star} + \rho_{0\text{m}} a^2 \left[\dot{D}_{\text{m}}^{\text{p}} \left(f^{-1} - f^{-2/3} \right) + (D_{\text{m}}^{\text{p}})^2 \left(3f^{-1} - \frac{5}{2} f^{-2/3} - \frac{1}{2} f^{-2} \right) \right]. \tag{20}$$

$$\boldsymbol{\Sigma}' = \boldsymbol{\Sigma}^{\star\prime}, \ \Sigma_{\text{eq}} = \Sigma_{\text{eq}}^{\star}. \tag{21}$$

The second term of the right hand side of Eq. (20) corresponds to the theory proposed by Carroll & Holt (1972) for porous materials and found also in Carroll et al. (1986) for the rapid compaction of powders.

2.2.3. *Viscoplastic contribution*

The quasistatic stress $\boldsymbol{\Sigma}^{\star}$, which includes viscous rate dependence, is evaluated using the Gurson-Tvergaard-Needleman (GTN) based viscoplastic flow surface (Gurson, 1977; Tvergaard, 1981; Needleman & Tvergaard, 1991):

$$\Omega\left(\boldsymbol{\Sigma}^{\star}, \bar{\sigma}, f\right) = \left(\frac{\Sigma_{\text{eq}}^{\star}}{\bar{\sigma}} \right)^2 + 2q_1 f \cosh\left(\frac{3}{2} q_2 \frac{\Sigma_{\text{m}}^{\star}}{\bar{\sigma}} \right) - \left[1 + (q_1 f)^2 \right] = 0\,, \tag{22}$$

with q_1, q_2 parameters, $\Sigma_{\text{m}}^{\star} = \dfrac{1}{3}\text{tr}(\boldsymbol{\Sigma}^{\star})$ and $\Sigma_{\text{eq}}^{\star} = \sqrt{\frac{3}{2}\boldsymbol{\Sigma}^{\star\prime} : \boldsymbol{\Sigma}^{\star\prime}}$, $\boldsymbol{\Sigma}^{\star\prime}$ being the deviatoric part of $\boldsymbol{\Sigma}^{\star}$.

The macroscopic plastic strain rate $\mathbf{D}^{\text{p}}$ and the stress tensor $\boldsymbol{\Sigma}^{\star}$ are related by the flow law:

$$\mathbf{D}^{\text{p}} = \dot{\kappa} \frac{\partial \Omega(\boldsymbol{\Sigma}^{\star}, \bar{\sigma}, f)}{\partial \boldsymbol{\Sigma}^{\star}}\,, \tag{23}$$

where $\Omega(\boldsymbol{\Sigma}^{\star}, \bar{\sigma}, f)$, characterizing the flow surface $\Omega(\boldsymbol{\Sigma}^{\star}, \bar{\sigma}, f) = 0$, is given by classical homogenization approaches (without micro-inertia). $\dot{\kappa}$ is the plastic multiplier

subject with Ω to the Kuhn-Tucker complementary conditions: $\Omega \leq 0$, $\dot{\kappa} \geq 0$, $\Omega\dot{\kappa} = 0$ (Simo & Hughes, 1998). It is obtained from the equivalence between the plastic work rate of the porous medium and the matrix dissipation rate:

$$\dot{\kappa} = \frac{2}{3}\frac{(1-f)\bar{\sigma}\Phi}{\boldsymbol{\Sigma}^\star : \frac{\partial \Omega}{\partial \boldsymbol{\Sigma}^\star}}\,. \tag{24}$$

$\bar{\sigma}$ is an average effective stress in the matrix, $\Phi = \Phi(\bar{\sigma}, \gamma^{\mathrm{p}})$ is the plastic shear strain rate defined by $\Phi = \frac{3}{2}d^{\mathrm{eq}}$ where d^{eq} is the equivalent plastic strain rate (assumed uniform) in the matrix. From Eqs (5, 22-24), one has:

$$\frac{\dot{\lambda}_1^{\mathrm{p}}}{\lambda_1^{\mathrm{p}}} = -\frac{(1-f)\,\Phi\left[\frac{2\Sigma_{\mathrm{eq}}^\star}{\bar{\sigma}} + q_1 q_2 f \sinh\left(-\frac{3}{2}q_2\frac{\Sigma_{\mathrm{m}}^\star}{\bar{\sigma}}\right)\right]}{3\left[\left(\frac{\Sigma_{\mathrm{eq}}^\star}{\bar{\sigma}}\right)^2 + \frac{3\Sigma_{\mathrm{m}}^\star}{2\bar{\sigma}}q_1 q_2 f \sinh\left(\frac{3}{2}q_2\frac{\Sigma_{\mathrm{m}}^\star}{\bar{\sigma}}\right)\right]} \tag{25}$$

and:

$$\frac{\dot{f}}{1-f} = -\frac{(1-f)\,\Phi q_1 q_2 f \sinh\left(-\frac{3}{2}q_2\frac{\Sigma_{\mathrm{m}}^\star}{\bar{\sigma}}\right)}{\left(\frac{\Sigma_{\mathrm{eq}}^\star}{\bar{\sigma}}\right)^2 + \frac{3\Sigma_{\mathrm{m}}^\star}{2\bar{\sigma}}q_1 q_2 f \sinh\left(\frac{3}{2}q_2\frac{\Sigma_{\mathrm{m}}^\star}{\bar{\sigma}}\right)}. \tag{26}$$

For Φ we adopt the expression proposed by Clifton (1970) for the viscoplastic dynamic response of aluminum under shock conditions:

$$\Phi = K_1(1 + K_2\gamma^{\mathrm{p}})\left(\frac{\langle\bar{\sigma} - \bar{\sigma}_a\rangle}{2T_1^\star}\right)^M \tag{27}$$

with $\langle\bullet\rangle = \frac{|\bullet|+\bullet}{2}$, K_1, K_2, M and $T_1^\star$ being material parameters which have been fitted by Clifton (1970), see Table 1. γ^{p} is a measure of the plastic strain defined as:

$$\gamma^{\mathrm{p}} = \int \Phi dt\,. \tag{28}$$

With this model, viscoplastic flow occurs when $\bar{\sigma} > \bar{\sigma}_a$, $\bar{\sigma}_a$ being the rate independent yield strength of the matrix. As in Clifton (1970), Molinari & Ravichandran (2004) and Czarnota et al. (2017), we adopt a power law to describe strain hardening in the matrix:

$$\bar{\sigma}_a = \sigma_{a0}\left[1 + \left(\frac{\gamma^{\mathrm{p}}}{\gamma_0}\right)^{1/n}\right], \tag{29}$$

where σ_{a0}, γ_0 and n are material parameters.

Note that the set of equations (27-29) has proven its ability to reproduce shock wave experiments in dense aluminum, Molinari & Ravichandran (2004). Note also

that this class of constitutive laws, although being a class of simplified rate hardening laws (power law formulation of the matrix viscous rate dependence), is commonly used to get a useful insight about how strain localization processes are affected by material rate sensitivity. In our analysis, we keep unchanged the values of the parameters K_1, K_2 and $T_1^\star$ appearing in the phenomenological law Eq. (27). However, to evaluate the effect of rate sensitivity on the shock structure, a parametric analysis is performed by varying the value of the exponent M.

From Eq. (20), the dynamic contribution reveals a size dependence (through the square of the current void radius) and provides a dependence on the strain rate $D_{\rm m}^{\rm p}$ and its time derivative $\dot{D}_{\rm m}^{\rm p}$. Both are bringing an additional rate dependence to the one already present in viscous effects carried out by $\Sigma_{\rm m}^\star$. The influence of $\left(D_{\rm m}^{\rm p}\right)^2$ and $\dot{D}_{\rm m}^{\rm p}$ appear as a specific signature of micro-inertia effects. Therefore, steady plastic shock waves are modulated by the interplay of the two rate dependencies respectively related to matrix viscosity and micro-inertia. This interaction needs to be explored.

3. Steady state plastic shocks

3.1. Shock path

We consider now the quasistatic compression curve, denoted by $\mathscr{C}_Y$, Fig. 2, which can be used in place of the Hugoniot for the analysis of shocks of moderate amplitudes (up to 8GPa for porous aluminum), see Czarnota et al. (2017). The quasistatic response defining $\mathscr{C}_Y$ is governed by the GTN rate independent yield surface since rate effects vanish at very slow loading. In such a circumstance, $\boldsymbol{\Sigma}^{\rm dyn}=\mathbf{0}$, $\boldsymbol{\Sigma}=\boldsymbol{\Sigma}^\star$, and the yield surface (denoted by Ω_a in this case) is obtained from Eq. (22) after replacing $\boldsymbol{\Sigma}^\star$ by $\boldsymbol{\Sigma}$ and $\bar{\sigma}$ by $\bar{\sigma}_a$ given by Eq. (29):

$$\Omega_a=\Omega\left(\boldsymbol{\Sigma},\bar{\sigma}_a,f\right)=\left(\frac{\Sigma_{\rm eq}}{\bar{\sigma}_a}\right)^2+2q_1f\cosh\left(\frac{3}{2}q_2\frac{\Sigma_{\rm m}}{\bar{\sigma}_a}\right)-\left[1+(q_1f)^2\right]=0\,. \quad (30)$$

Note that the original Gurson yield function was considered and the following values have been adopted $q_1=q_2=1$.

Planar impacts are considered and it is assumed that a plastic steady shock wave is formed beyond a certain propagation distance. Also, the analysis is restricted to

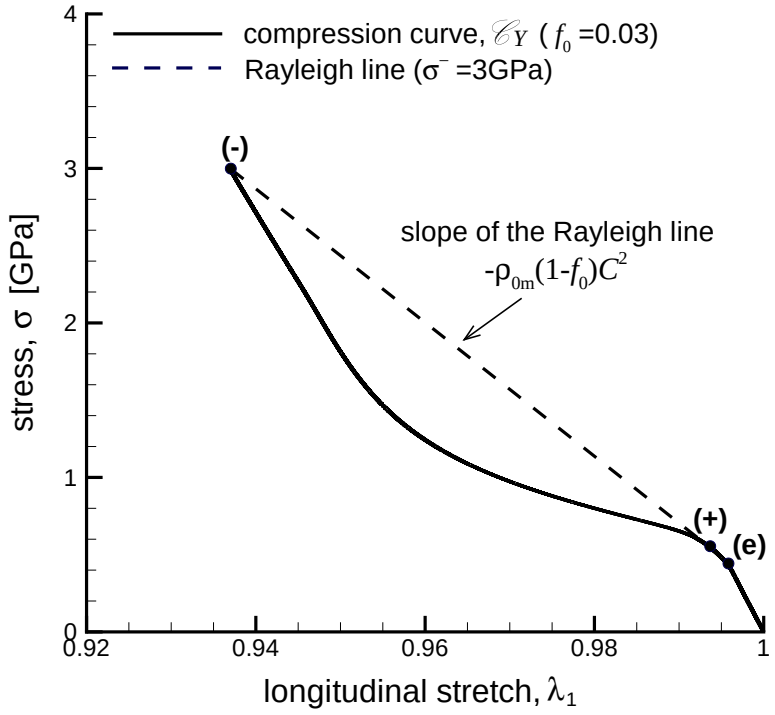

Figure 2: Quasistatic compression curve $\mathscr{C}_Y$ for porous aluminum ($f_0 = 0.03$, other material parameters listed in Table 1) and Rayleigh line defining the shock path from state (+) to state (-) for σ^-=3GPa (C=4 059m/s). The Rayleigh line, of slope $-\rho_{0\mathrm{m}}(1-f_0)C^2$ is tangent to $\mathscr{C}_Y$ at state (+) and intersects $\mathscr{C}_Y$ at state (-). From state (e), corresponding to the first plastic yielding, to state (+), state variables are varied following the compression curve $\mathscr{C}_Y$. For this example, $(\lambda_1^{\mathrm{e}}, \sigma^{\mathrm{e}})$=(0.99593, 0.428GPa) and (λ_1^+, σ^+)=(0.99367, 0.547GPa).

shocks of moderate amplitudes and temperature effects are disregarded. The reader is referred to Molinari & Ravichandran (2004) for further comments on dense materials and Czarnota et al. (2017) for the case of porous materials.

Upon impact, a first elastic wave is triggered compressing the material particles from the initial state to state (e), corresponding to the first plastic yielding. Then, a plastic fan may occur, compressing material particles up to state (+). The plastic fan is followed by a plastic shock compressing further more the material up to state (-). Fig. 2 gives an example of a quasistatic compression curve obtained for porous aluminum ($f_0 = 0.03$) with locations of state (e) as well as states (+) and (-) when σ^-=3GPa.

Let us now consider an observer attached to the steady plastic shock wave moving at the constant Lagrangian speed C. For this observer, the shock structure remains constant and one can express all variables in terms of the moving coordinate ξ defined by:

$$\xi = X - Ct\,, \tag{31}$$

with $\xi = +\infty$ and $\xi = -\infty$ corresponding respectively to state (+) ahead and to the state behind the plastic shock layer.

Using Eq.(31), Eqs (9-10) are written as:

$$\frac{dT_1}{d\xi} = -\rho_{0\mathrm{m}} C\,(1-f_0)\,\frac{dv}{d\xi}\,, \tag{32}$$

$$\frac{dv}{d\xi} = -C\frac{d\lambda_1}{d\xi}\,. \tag{33}$$

Upon integration with respect to ξ from state (+), any state within the plastic shock layer verifies the following relationships:

$$T_1 - T_1^+ = -\rho_{0\mathrm{m}} C\,(1-f_0)\left(v - v^+\right)\,, \tag{34}$$

$$v - v^+ = -C\left(\lambda_1 - \lambda_1^+\right)\,. \tag{35}$$

By combining Eqs (34) and (35) and using the compressive stress $\sigma = -T_1$, one establishes the equation of the Rayleigh line

$$\sigma - \sigma^+ = -\rho_{0\mathrm{m}} C^2\,(1-f_0)\left(\lambda_1 - \lambda_1^+\right)\,. \tag{36}$$

The Rayleigh line (Eq.36), which defines the shock path, is entirely characterized from the quasistatic compression curve $\mathscr{C}_Y$ jointly with the chord criterion. From this, the Rayleigh line is tangent to the compression curve $\mathscr{C}_Y$ at state (+) defined by (λ_1^+, $\sigma^+ = \sigma_{\mathscr{C}}(\lambda_1^+)$) and intersects $\mathscr{C}_Y$ at state (-) characterized by (λ_1^-, $\sigma^- = \sigma_{\mathscr{C}}(\lambda_1^-)$), see Fig. 2.

From Eq. (36) written at state (-), we obtain:

$$\sigma^- - \sigma^+ = \sigma_{\mathscr{C}}(\lambda_1^-) - \sigma_{\mathscr{C}}(\lambda_1^+) = -\rho_{0\mathrm{m}} C^2 \left(1 - f_0\right) \left(\lambda_1^- - \lambda_1^+\right) . \tag{37}$$

which defines the Rayleigh line from state (+) to state (-) along which we investigate the steady shock structure. Note that a one to one correspondence exists between C and σ^- so that a shock can be characterized by its celerity or the stress level at state (-).

The stretch and stress at state (+), respectively λ_1^+ and σ^+, are characterized from the compression curve and the chord criterion. All other quantities at state (+) are determined assuming that viscous and micro-inertia effects are playing no role along the fan structure. Therefore, evolutions of the plastic stretch and porosity can be evaluated along the compression curve from state (e) to state (+) (see Czarnota et al., 2017, for details). Besides, using Eqs (32-33) where C is replaced by the instantaneous fan velocity $\sqrt{\frac{dT_1/d\lambda_1}{\rho_{0\mathrm{m}}(1-f_0)}}$, the corresponding particle velocity v^+ is obtained:

$$v^+ = v^{\mathrm{e}} - \int_{(\mathrm{e})}^{(+)} \sqrt{\frac{dT_1/d\lambda_1}{\rho_{0\mathrm{m}}\left(1 - f_0\right)}} d\lambda_1 \, , \tag{38}$$

where $\frac{dT_1}{d\lambda_1} = -\frac{d\sigma_{\mathscr{C}}}{d\lambda_1}(\lambda_1)$ is calculated from the compression curve $\mathscr{C}_{\mathrm{Y}}$. v^{e} is the particle velocity due to the elastic shock obtained from relationships similar to Eqs (32-33):

$$v^{\mathrm{e}} = C^{\mathrm{e}} \left(1 - \lambda_1^{\mathrm{e}}\right) , \tag{39}$$

$$C^{\mathrm{e}} = \sqrt{\frac{-T_1^{\mathrm{e}}}{\rho_{0\mathrm{m}} \left(1 - f_0\right) \left(1 - \lambda_1^{\mathrm{e}}\right)}} \, , \tag{40}$$

with C^{e} being the elastic shock wave velocity. The elastic state and corresponding values of λ_1^{e} and $-T_1^{\mathrm{e}}$ are identified from Eqs (13-15) and (30) with $f = f_0$, $\bar{\sigma}_a = \sigma_{a0}$, $\varepsilon_1^{\mathrm{e}} = \lambda_1^{\mathrm{e}} - 1$ and $\varepsilon_2^{\mathrm{e}} = 0$. The knowledge of state (e) allows to calculate v^+ with Eq. (38).

3.2. Relationship between shock speed C and particle velocity v^-

The relationship between the plastic shock speed C and the particle velocity v^- at state (-) is a fundamental outcome of plate impact experiments. In our approach, this relationship is obtained from the shock path and thus, as described above, only relies on the quasi-static compression curve $\mathscr{C}_Y$. The present modeling has been accurately compared to experimental data of the literature, collected for various initial porosities and shock stresses, Czarnota et al. (2017). Particularly, due to porosity, a nonlinear relationship between shock velocity and impact velocity is obtained which deviates from the linear law usually obtained for steady plastic shocks in polycristalline metals.

While the problem has been addressed by numerical solving of the governing equations in Czarnota et al. (2017) we propose in Appendix A an approximate analytical solution for the $C - v^-$ curve able to reproduce experimental data with the same accuracy.

4. Structure of plastic shocks in porous materials

4.1. Shock structure

Once the states (+) and (-) are identified (see section 3.1), the shock structure, characterized here by the variation of the total accumulated plastic strain with respect to the lagrangian position ξ, is obtained from a nonlinear system of differential equations. When micro-inertia is disregarded, $\Sigma^\star_{\rm eq} = \Sigma_{\rm eq}$, $\Sigma^\star_{\rm m} = \Sigma_{\rm m}$ and this system of equations is deduced from Eqs (28) and (25-26). In presence of micro-inertia, Eqs (20, 28, 25) are used. More details on the integration scheme are presented in Appendix B.

Note that when micro-inertia is disregarded, the equilibrium state, defined as producing a nil plastic flow rate (Φ=0), is reached at state (-). As a consequence, σ^- is equal to the equilibrium stress $\sigma^{\rm rear}$ at the rear of the plastic shock front. When micro-inertia is accounted for, it appears that σ^- is not in general the equilibrium stress because of a residual microscale kinetic energy that may still be present at state (-). However, it appears that for moderate shock amplitudes as considered here, σ^- can be taken as a good approximation of the equilibrium stress $\sigma^{\rm rear}$ even in presence of micro-inertia, see Czarnota et al. (2017).

4.1.1. Influence of the strain rate sensitivity

In this section, micro-inertia is therefore disregarded and the effect of the strain rate sensitivity on the shock structure is analyzed by varying the parameter $M = 1/m$, m being the strain rate sensitivity, see Eq. (27). All material parameters adopted here are representative of a porous aluminum, see Table 1.

Fig. 3 shows the profile of the accumulated plastic strain $E^{\rm p}_{\rm eq}$ within the shock for f_0=0.03. Calculations were made for M=1.25, 1.78, 3 and for two stress amplitudes σ^-=3GPa, i.e. C=4 059m/s (Fig. 3-a) and 5GPa, i.e. C=4 686m/s (Fig. 3-b). Note that all profiles are centered at ξ=0, standing for the location within the shock where the plastic strain rate $D^{\rm p}_{\rm eq}$ is maximum. When micro-inertia is disregarded, the equilibrium stress (reached when no more plasticity is accumulated) is identified by σ^- on the quasi-static compression curve $\mathscr{C}_Y$ which is independent of the viscous part of the material response. As a consequence, the total accumulated plastic strain $E^{\rm p-}_{\rm eq}$ is not affected by M. However, the shock structure itself is highly influenced by the viscous contribution. The shock profile appears to broaden as M is decreased which is the manifestation of the stabilizing effect of the matrix rate sensitivity. Finally, by comparing Fig. 3-a to Fig. 3-b, one also notices a narrower shock structure when σ^- is increased for a fixed value of M. This will be explored in more details in a forthcoming section.

The shock profile is now analyzed with Fig. 4 giving $D^{\rm p}_{\rm eq}$ versus position ξ for M=1.25, 1.78, 3, considering σ^-=3GPa (Fig. 4-a) and σ^-=5GPa (Fig. 4-b). The bell-shaped shock structure appears as non symmetric with respect to ξ=0. This trend, commented in Czarnota et al. (2017), is attributed to the void closure process partly dictated by the value of the initial porosity. For dilute materials (low initial porosity), the shock structure shows a highly symmetric shape commonly observed in dense materials, see Czarnota et al. (2017). Figs 4-a and-b also confirm the strong effect of the strain rate sensitivity. The influence of M is particularly marked on Fig. 4-b where σ^-=5GPa. By reducing M from 3 to 1.25, i.e. by increasing the strain rate sensitivity $m = 1/M$ from 0.33 to 0.8, the drop in maximum value of $D^{\rm p}_{\rm eq}$ is about four decades of strain rate.

Also, note the peculiar behavior revealed for M=1.25 on Fig. 4-b. In fact, the com-

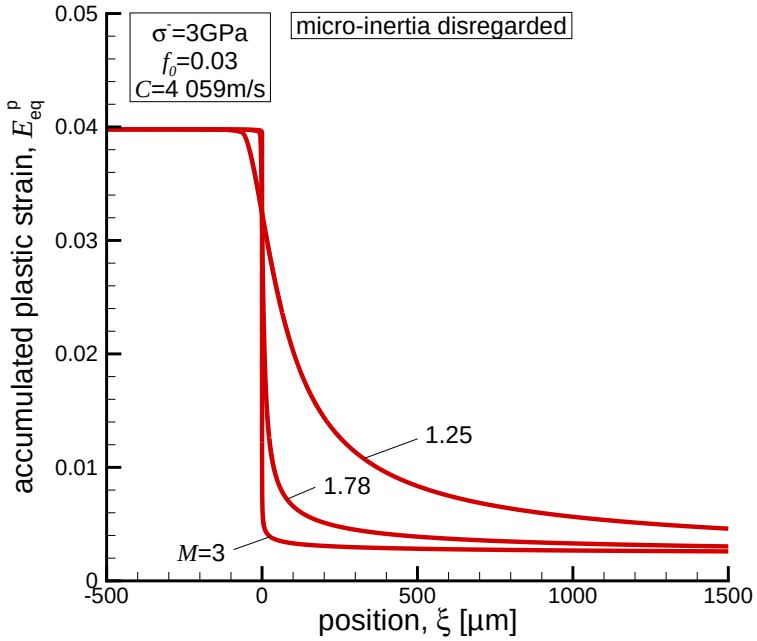

a)

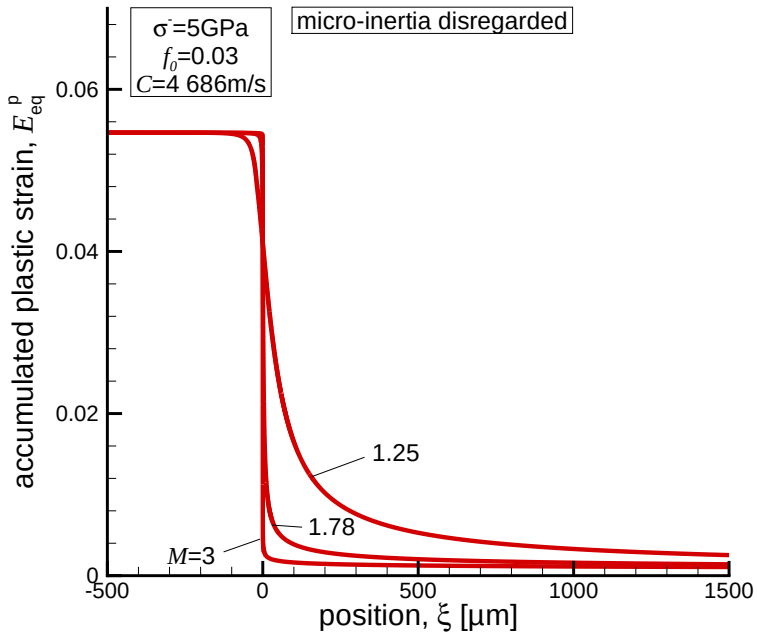

b)

Figure 3: Accumulated plastic strain $E^{\mathrm{p}}_{\mathrm{eq}}$ versus position ξ for porous materials of initial porosity f_0=0.03 and for a stress amplitude σ^- of: a) 3GPa (corresponding shock speed C=4 059m/s); b) 5GPa (corresponding shock speed C=4 686m/s). Micro-inertia is disregarded while various values of the strain rate parameter M are considered (all other parameters are listed in Table 1).

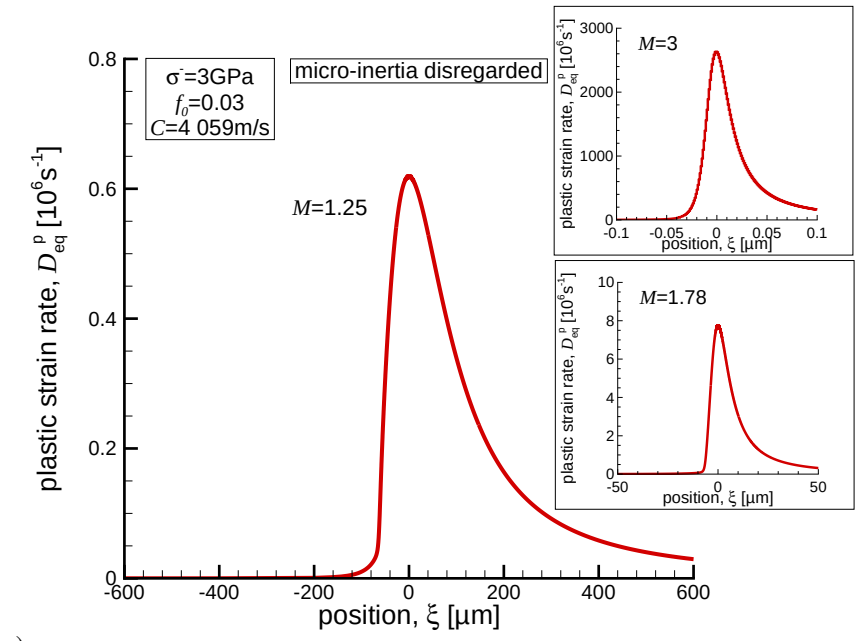

a)

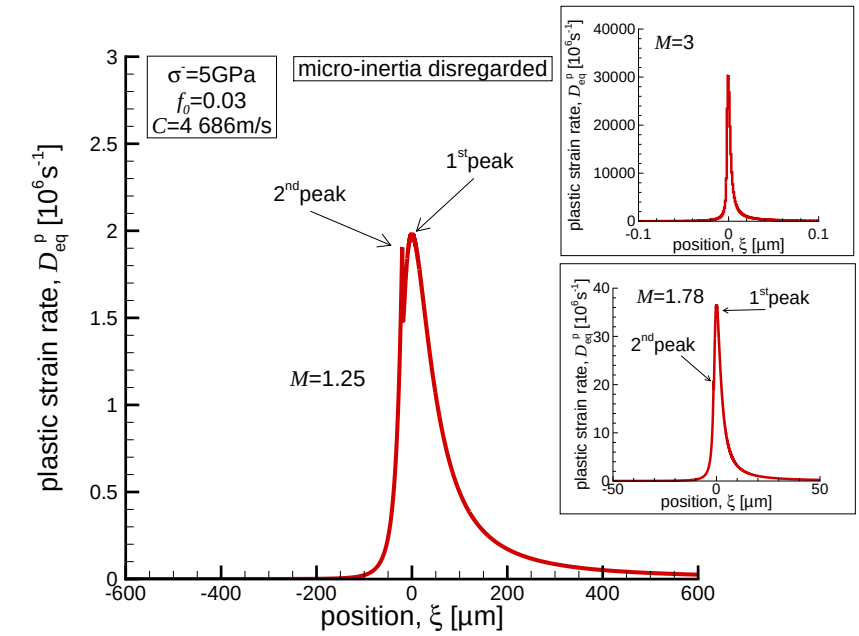

b)

Figure 4: Equivalent plastic strain rate $D^{\mathrm{p}}_{\mathrm{eq}}$ versus position ξ for initial porosity f_0=0.03 and for a stress amplitude σ^- of :a) 3GPa (corresponding shock speed C=4 059m/s); b) 5GPa (corresponding shock speed C=4 686m/s). Micro-inertia is disregarded while various values of the strain rate parameter M are considered (all other parameters are listed in Table 1)

puted bell-shaped structure is disturbed within a very small region (between -23μm and -19μm) where a second peak (starting from $\xi = +\infty$) in $D^{\mathrm{p}}_{\mathrm{eq}}$ emerges. This reflects a change in the kinetics of the compression process. While the first peak occurs at the late stage of the pore closure process, the second peak is related to the dense matrix behavior after pore closure. One should mention that it exists also for M=1.78 and disappears for M=3. In addition, it appeared (results not shown here) that the second localization of the strain rate leads to a higher peak for low M and large σ^- whereas the porosoty f_0 was found to have a minor effect.

The shock structure thus exhibits two localization zones for the strain rate. This trend might suggest the appearance of a sub-shock generally predicted by hyperbolic dissipative systems. For these cases, the shock structure may reveal a discontinuous part (sub-shock) occurring when the velocity of the shock wave is greater than a critical value, Taniguchi & Ruggeri (2018). Here, however, we have rather identified a quasi sub-shock since the shock structure is not discontinuous. Moreover, we note that the second localization stage is of very low intensity in terms of plastic strain accumulated over its extent (the area below the second peak in the graph $D^{\mathrm{p}}_{\mathrm{eq}}(\xi)$ is negligible). To the authors knowledge, the presence of the second peak has never been revealed for porous materials in the literature. This is probably related to its nature (tiny extend of the disturbed region), and the fact that it leaves no trace on the shock structure of Fig. 3. It is believed that this second peak is hardly detectable in experiments.

4.1.2. Viscous/micro-inertia combined effects

Micro-inertia is now included in the calculation so that the initial void size a_0 plays a role in the structure of the shock wave. Remind that in presence of micro-inertia, σ^- may not coincide with the equilibrium stress σ^{rear}, because of the micro-scale kinetic energy that may remain at state (-). As in Czarnota et al. (2017), the aim is not to analyze the entire shock layer. Shock structures will be displayed up to σ^- completed with a schematic dashed line, as represented in the forthcoming Fig. 5.

The case where M is fixed and a_0 is varied has been analyzed in Czarnota et al. (2017). It appeared that the stabilizing effect of micro-inertia, enhanced as a_0 is increased, leads to a broadening of the shock structure and a reduction of the strain rate

level within the shock, see Figs 9-10 of Czarnota et al. (2017).

The interplay of viscous and micro-inertia effects is illustrated in this section for f_0=0.03 and σ^-=5GPa (shock speed C=4 686m/s). Fig. 5 shows the evolution of $E^{\mathrm{p}}_{\mathrm{eq}}$ in terms of ξ for M=1.25 and 3, considering the case of an initial void radius a_0=50μm. For comparison purpose, the corresponding micro-inertia independent results (i.e. $a_0 \to 0$) of Fig. 3 is superimposed. Clearly, micro-inertia effects enter into play for both values of M with particular marked influence when M=3 (i.e. low strain rate sensitivity). For this value of M, the widespread shock structure obtained with large voids contrasts with the one observed when micro-inertia is disregarded. The later develops in a very thin layer, exhibiting a quasi-discontinuous shape.

In fact, two situations emerge from Fig. 5. For small initial void radius, when $a_0 \to 0$, the shock structure is not influenced by micro-inertia and is strongly modulated by viscous effects. By contrast, for large initial void size, micro-inertia effects are important and viscous effects become relatively less pronounced.

4.2. Shock layer width

As in Molinari & Ravichandran (2004) and Czarnota et al. (2017), the extension of the shock layer is characterized by a single parameter, the shock layer width denoted by w in the following. Somehow, w is aimed to characterize the width of the core of the shock layer where most of the variation of the accumulated plastic strain is taking place. This characterization will be useful to get a clearer view of the role of micro-inertia and matrix viscosity on the shock structure.

In some cases, see for instance Fig. 4, the maximum of the plastic strain rate within the shock occurs at a second peak with a value that can be larger than the one observed at the first peak. However, the second peak prevails on a tiny part of the shock structure and cannot be used to define a characteristic of the shock extent. As a consequence, in this paper, the shock layer width w is adapted from Czarnota et al. (2017) and is defined as:

$$w = \frac{C\Delta E^{\mathrm{p}}_{\mathrm{eq}}}{D^{\mathrm{p}}_{\mathrm{eq\ (1st\ peak)}}}\,, \tag{41}$$

where $\Delta E^{\mathrm{p}}_{\mathrm{eq}} = E^{\mathrm{p}-}_{\mathrm{eq}} - E^{\mathrm{p}+}_{\mathrm{eq}}$ is the variation of the accumulated plastic strain across the shock. Recall that $D^{\mathrm{p}}_{\mathrm{eq\ (1st\ peak)}}$ is the first maximum in $D^{\mathrm{p}}_{\mathrm{eq}}$ reached starting from

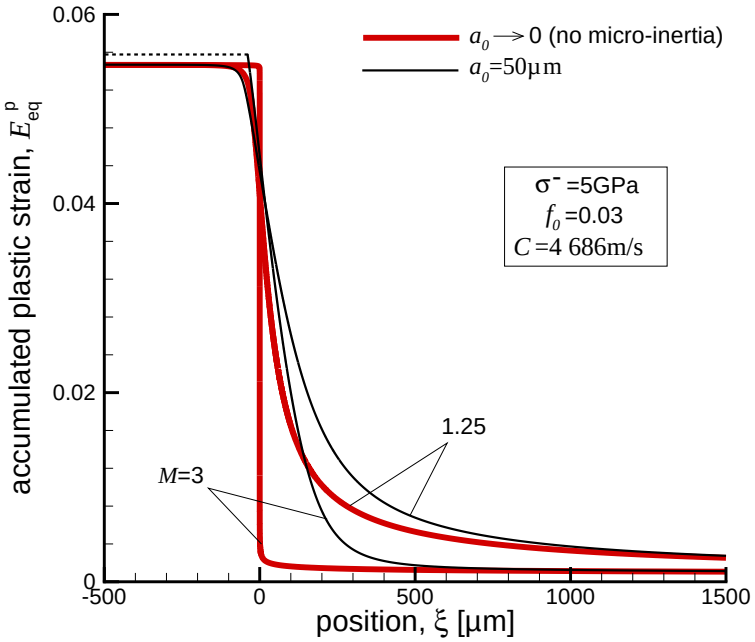

Figure 5: Accumulated plastic strain $E^{\mathrm{p}}_{\mathrm{eq}}$ versus position ξ for porous materials of initial porosity f_0=0.03. The stress amplitude is σ^-=5GPa (corresponding shock speed C=4 686m/s). Micro-inertia dependent (with a_0=50μm) and micro-inertia independent predictions (i.e. $a_0 \rightarrow 0$) are superimposed for two values of the strain rate parameter: M=1.25 and 3. All other parameters are listed in Table 1.

$\xi = +\infty$.

Figs 6a and b show the dependence of the shock layer width w with respect to M for σ^-=5GPa and various values of the initial porosity. The dense material response is also provided. Let first concentrate on the situation of small radius where micro-inertia is negligible, i.e. $a_0 \to 0$ for which the shock structure is strongly influenced by viscous effects. In that case, Fig. 6a shows that the shock layer width w is reduced when f_0 is enlarged. In addition, for a given initial porosity, w shows a linear dependence with respect to M in the semilog scaling of Fig. 6a. This result, obtained by Molinari & Ravichandran (2004) for dense materials, is observed here for porous materials containing small voids ($a_0 \to 0$) so that micro-inertia effects are negligible.

The micro-inertia contribution is included in Fig. 6b for an initial void size a_0=50μm. It is confirmed that micro-inertia effects become more important as M is increased (small rate sensitivity $m = 1/M$), see also Fig. 5. When M=1, the shock layer width falls close to the micro-inertia independent results of Fig. 6a whatever the initial porosity. As a consequence, when the strain rate sensitivity m is large, the micro-inertia effects are small and w is shown to increase with f_0. However the shock layer width w obtained with the complete theory can be much larger than the micro-inertia independent result for $M \geq$1.78, especially when $f_0 \geq$0.003. A particular consequence of micro-inertia is that the dependence of w on f_0 appears to be non monotonic when a_0=50μm. Note that even if they are limited in the case of very low f_0, micro-inertia effects lead to a larger shock layer width in the porous material than in the dense material when $M \geq$1.78. This result, observed for all tested values of the initial porosity, is extending the findings of Czarnota et al. (2017). Finally, when $f_0 \geq$0.03, Fig. 6b shows that the shock layer width becomes slightly dependent on M for $M \geq$1.78 and tends to an asymptotic value (plateau). This trend is observed when micro-inertia effects are important.

In order to develop a better understanding of the interplay between viscous and micro-inertia effects, we propose to focus on the results obtained for f_0=0.03 and bring further information. The shock layer width is displayed in terms of M in Fig. 7a for two initial void sizes, a_0=12.5 and 50μm and for σ^-=5GPa. The results without micro-inertia ($a_0 \to 0$) are also reported. It is shown that the difference between the

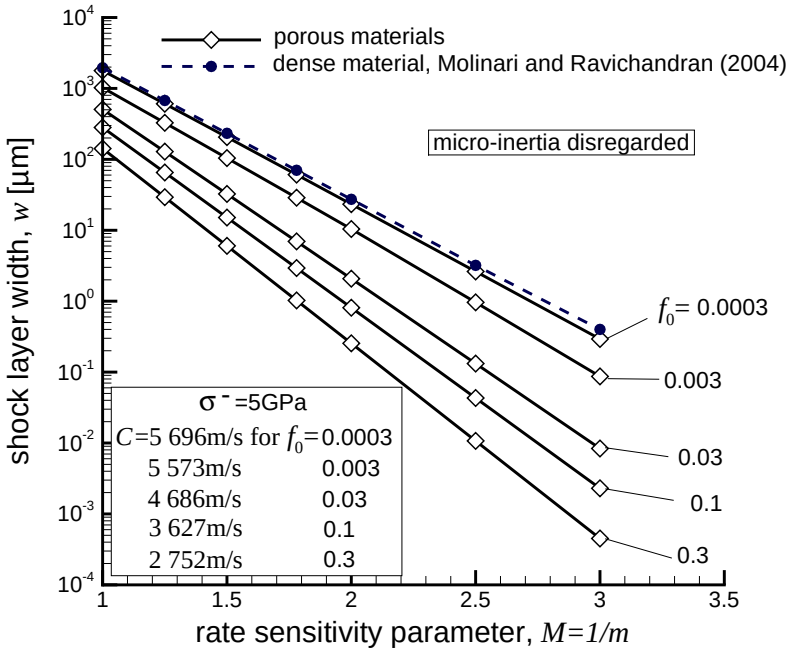

a)

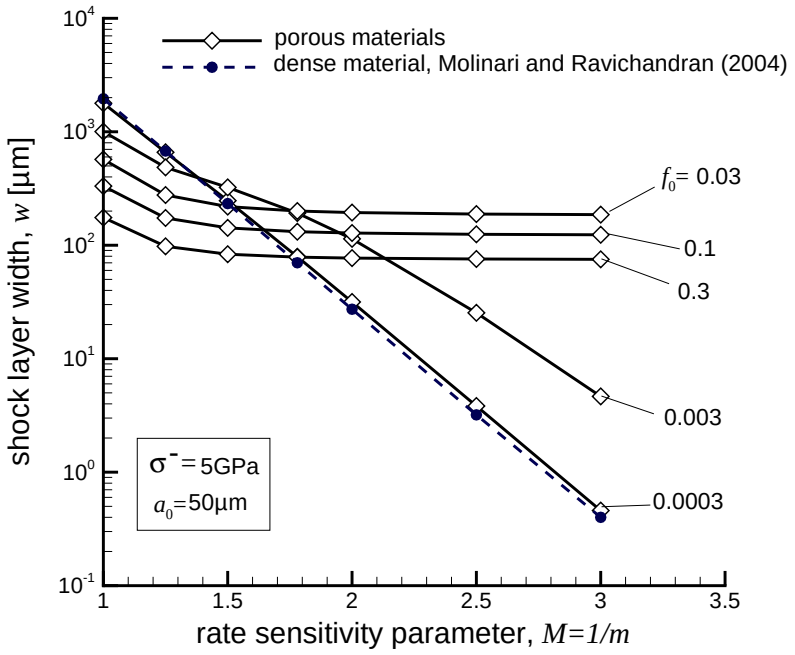

b)

Figure 6: Shock layer width w in terms of the inverse of the strain rate sensitivity $M = 1/m$ for various initial porosities (semilog scale). The shock stress is σ^-=5GPa: a) Micro-inertia is neglected; b) Micro-inertia is included considering an initial void radius a_0=50μm.

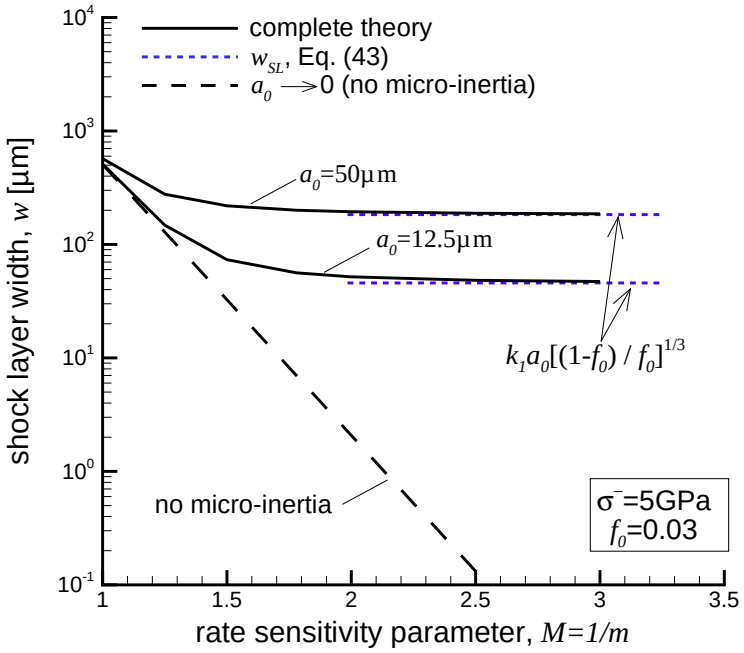

a)

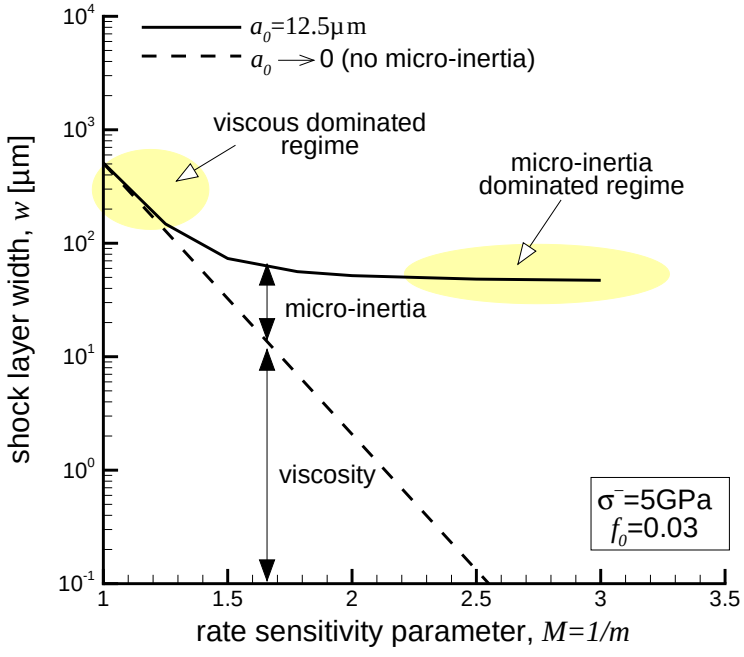

b)

Figure 7: Shock layer width w in terms of the inverse of the strain rate sensitivity $M = 1/m$ for f_0=0.03 (semilog scale). The shock stress is σ^-=5GPa. The micro-inertia independent ($a_0 \rightarrow 0$) and the complete theory with a_0=12.5 and 50μm are provided in a) while the cases $a_0 \rightarrow 0$ and a_0=12.5μm are used in b) to highlight two regimes of dominant effects. Results in the micro-inertia dominated regime can be described by $w = k_1 a_0 \left(\frac{1-f_0}{f_0}\right)^{1/3}$ with k_1=1.15, see Czarnota et al. (2017).

micro-inertia independent approach and the complete theory is enhanced when a_0 is increased, characterizing the stronger effect of micro-inertia when the initial void size is larger.

The case f_0=0.03, σ^-=5GPa with a_0=12.5μm and the corresponding micro-inertia independent theory is now illustrated to highlight two regimes controlling the shock structure. From the semi-log scaling of Fig. 7b, the viscous dominated domain is shown to cover the range $1 \leq M \leq$1.25 (negligible contribution of micro-inertia to the shock layer width w). Within that domain, the shock layer width strongly depends on the viscous effects. By contrast, when $M \geq$2, it appears that the shock layer width is slightly dependent on M. This trend clearly characterizes the micro-inertia dominated regime, where w results mainly from the micro-inertia effects and is not influenced by viscous effects. For instance, when M=2.5 on Fig. 7b, the contribution of the matrix viscosity to w is given by 0.13μm while the contribution of micro-inertia is 51.8μm. Fig. 7a is complemented by the prediction of the scaling law proposed by Czarnota et al. (2017), obtained from a dimensionless analysis and valid when micro-inertia effects are important. We designate by w_{SL} the shock layer width obtained from this approximation, see Eq. (69) in Czarnota et al. (2017):

$$w_{\text{SL}} = k_1 a_0 \left(\frac{1 - f_0}{f_0} \right)^{1/3}, \tag{42}$$

where k_1 is a parameter depending on the matrix properties, including M. Note that the authors have restricted their study to M=1.78 and identified k_1=1.15. When M is large (i.e. low strain rate sensitivity $m = 1/M$) it appears from Fig. 7a that w_{SL} is in agreement with the shock layer width w characterizing the micro-inertia dominated domain. Note that Eq. (42) could not be applied for very low values of f_0, since in this case micro-inertia effects are not important.

The effect of a_0 is also portrayed in Fig. 8 showing the evolution of the shock layer width versus initial void size ranging from 0 to 50μm. The initial porosity is still f_0=0.03 and the shock stress is σ^-=5GPa. We consider M=1.25 in Fig. 8a and M=3 in Fig. 8b. Due to the stabilizing effect of viscosity, the shock layer width appears larger for lower values of M (larger rate sensitivity $m = 1/M$). This trend, already depicted for $a_0 \rightarrow$0 and 50 μm and various initial porosities in Fig. 6b, is confirmed

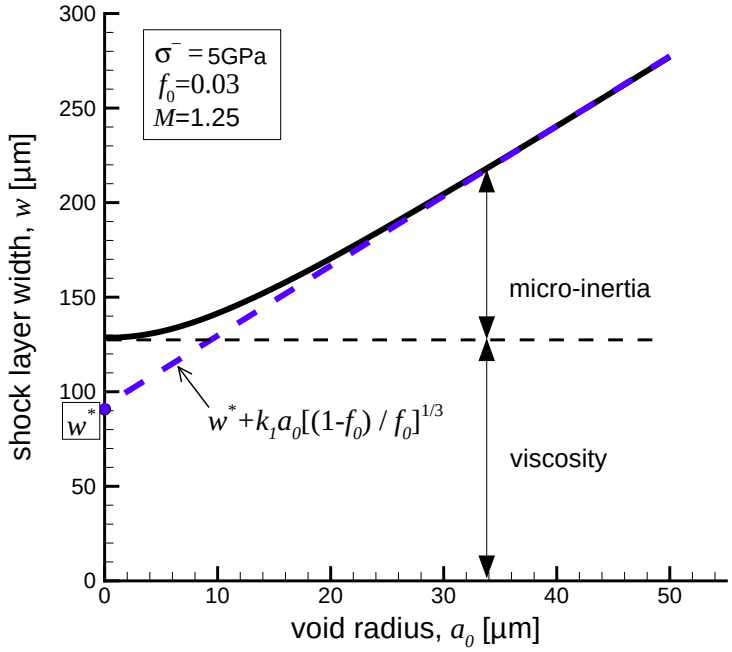

a)

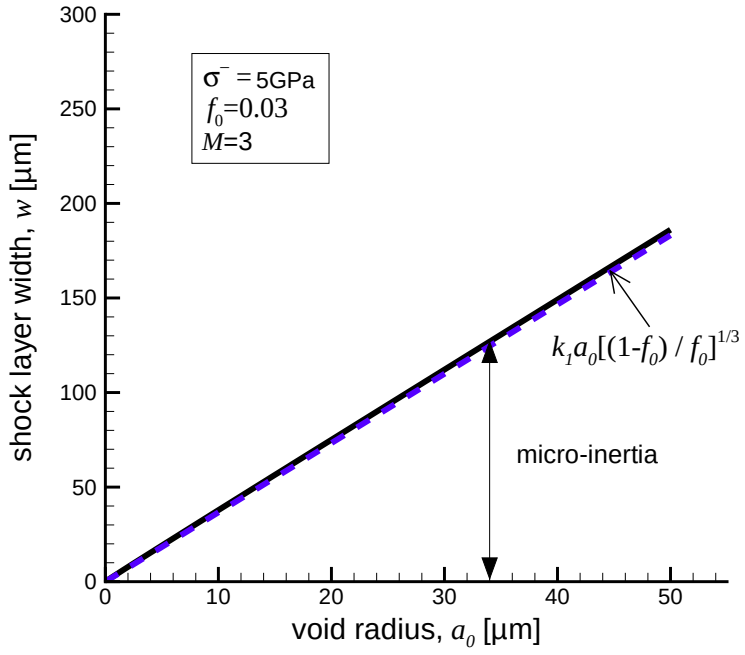

b)

Figure 8: Shock layer width w in terms of the initial void size a_0 when the inverse of the strain rate sensitivity is a) M=1.25 and b) M=3. The initial porosity is f_0=0.03, the shock stress is σ^-=5GPa. Note that for $M = 3$ (smaller rate sensitivity $m = 1/M$) the shock wave structure is governed by micro-inertia.

here for all values of a_0, f_0 being fixed. In addition, when $a_0 \neq 0$, the shock structure benefits from the stabilizing effect of micro-inertia, leading to the increase of w with a_0, confirming again previous trends. When M=1.25, i.e. for a large strain rate sensitivity, Fig. 8a shows that the shock layer width results from a combination of viscous and micro-inertia effects. In fact, w can be decomposed as:

$$w = w^* + w_{\mathrm{SL}} \tag{43}$$

where w_{SL} is given by Eq. (42) and w^* is micro-inertia independent. The aim of the present study is not to identify an explicit relationship for w^*. One can however note that w^* is shown to be a decreasing function of M, tending to vanish when the strain rate sensitivity parameter $m = 1/M$ vanishes, as shown in Fig. 8b obtained with M=3.

5. Relevance of the Swegle and Grady power law for porous aluminum

An interesting aspect related to steady plastic shock waves concerns the link between the stress jump across the shock and the maximum strain rate within the shock. Swegle & Grady (1985) revealed that the strain rate within a steady shock is related to the stress jump via a power law i.e. $\dot{\epsilon}_{\mathrm{SG}} = A\Delta\sigma^{h_{\mathrm{SG}}}$, where $\dot{\epsilon}_{\mathrm{SG}}$ has been defined by the authors as the ratio of the maximum time derivative of the particle velocity to the steady shock velocity. The coefficient A is material dependent and a value of the exponent h_{SG}=4 (fourth power law) was shown to be consistent for a large number of metals such as Al, Fe, Be, Bi, Cu and U, Swegle & Grady (1985). In addition, the authors related the exponent to the strain rate sensitivity m of materials under shock loading through $h_{\mathrm{SG}} = 2/m = 2M$. This result was revisited by Molinari & Ravichandran (2004) who derived, from a theoretical approach, a power law relationship connecting the stress jump to the maximum longitudinal plastic strain rate reached within the shock: $\max\left(D_{11}^{\mathrm{p}}\right) = B\Delta\sigma^{h_{\mathrm{MR}}^{\mathrm{p}}}$. A similar relationship was found when considering the total longitudinal strain rate D_{11} in place of D_{11}^{p}, the exponent now being h_{MR}. The exponents $h_{\mathrm{MR}}^{\mathrm{p}}$ and h_{MR} are also related to the strain rate sensitivity. Of most importance is that $h_{\mathrm{MR}}^{\mathrm{p}}$ and h_{MR} involve coefficients depending on material properties. As a matter of fact, all polycristalline metals are not expected to present the same strain

rate sensitivity. For dense aluminum, the authors obtained, see Eq (75) of Molinari & Ravichandran (2004):

$$h^{\mathrm{p}}_{\mathrm{MR}} = 1.87M + 0.663 \quad \text{and} \quad h_{\mathrm{MR}} = 1.87M + 0.620 \tag{44}$$

with M=1.78, one obtains $h^{\mathrm{p}}_{\mathrm{MR}} = 4$ and $h_{\mathrm{MR}} = 3.95$ which allow a good fit to experimental data, see Molinari & Ravichandran (2004). In Ding & Asay (2009), the plastic response is described by an overstress viscoplastic model where strain hardening, pressure and temperature dependences are also incorporated in the Swegle and Grady model, following the approach proposed by Steinberg et al. (1980). The Swegle and Grady scaling law is not restricted to power law formulation of the viscoplastic response and is retrieved for other classes of constitutive laws (e.g. Austin & McDowell, 2011, 2012, for a generalized Orowan relation which accounts for rate and path-dependent evolution of dislocation substructure in shock-loaded pure metals).

A power law relating the stress jump to the strain rate seems to be a common feature in shock experiments, the exponent being adjusted depending on materials under investigation. Strongly heterogeneous media have been investigated in the literature, and various studies do not display the fourth power law in general, Grady (2010). For instance, an exponent of 0.8 was revealed for steel-polymer bead chains, Molinari & Daraio (2009). Note that for this case, the shock wave is structured by dispersive effects. Dispersive effects are also the main contribution to the shock structuring in high contrasted laminate composites (e.g. steel-polymer composite, Molinari & Ravichandran, 2006, aluminum-tungsten composite, Franco Navarro et al.,2016). Using gradient plasticity theories, Molinari & Ravichandran (2006) found an exponent close to 1.8 which compares well to experimental data of Zhuang et al. (2003). The power law is also retrieved by Vogler et al. (2012) from experiments conducted on three classes of heterogeneous solids: layered, particulate composite, and granular. They particularly showed that a value of the exponent about 1 is consistent for granular materials considered in the study (WC$-$Co, SS, Al, Al_2O_3), and explained that the first power scaling in granular materials is due to the mass flow of material across voids.

Here, we consider porous metals where the shock wave is structured by viscous dissipative effects combined to micro-inertia effects. In the following we shall see that

a single power law of the following form:

$$\max\left(D_{11}^{\mathrm{p}}\right) = H\Delta\sigma^{h^{\mathrm{p}}} \tag{45}$$

is not able to characterize the shock response.

Fig. 9 shows the dependence of the stress jump $\Delta\sigma = \sigma^- - \sigma^+$ across the shock in terms of $\max\left(D_{11}^{\mathrm{p}}\right)$ in a log-log diagram. Several shock stress levels are considered, σ^-=1, 1.25, 1.5, 2, 3, 5 and 8GPa. The initial porosity is f_0=0.03 and the initial void radius adopts values ranging from 0.1 to 50μm. The strain rate parameter is M=1.78, corresponding to the value of the reference aluminum of Tab. 1 and studied elsewhere, Molinari & Ravichandran (2004) and Czarnota et al. (2017).

Let us first mention that the results obtained for a_0=0.1μm coincide with the micro-inertia independent calculation (dashed line). For this case, two regimes are schematically identified in Fig. 9: a first regime for $\Delta\sigma$<1.4GPa (σ^-<2GPa) where the relationship between stress jump and strain rate is a power law with an exponent near 4 and a second for $\Delta\sigma$>2.45 GPa (σ^->3GPa) with an exponent about 2.5. The effect of the initial porosity thus enters into play at large shock stress levels. At low stress level, h^{p} is close to $h_{\mathrm{MR}}^{\mathrm{p}}$=4, the value measured for dense aluminum.

The link between the stress jump and the strain rate is naturally influenced by the initial void size. Due to the stabilizing effect of micro-inertia, the plastic strain rate is reduced as a_0 is increased. As a consequence, a deviation from the micro-inertia independent calculation occurs when a_0 is large and at larger stress. Most interestingly is the slope revealed for a_0=12.5, 25 and 50 μm which seems to be independent from a_0 when a_0 is large enough. It will be further verified that in this configuration (corresponding to a regime dominated by micro-inertia) the slope $1/h^{\mathrm{p}}$ is depending on the initial porosity and that $1-f_0$ provides a good estimate of h^{p}, as reported in the log-log diagram of Fig. 9 obtained for f_0=0.03.

The influence of M is investigated in Fig. 10 for f_0=0.03 and a_0=50μm. When micro-inertia is neglected (dashed lines), the exponent $h_{\mathrm{MR}}^{\mathrm{p}}$, related to dense aluminum and depending on M (see Eq. 44), prevails for low shock stress levels until the effect of porosity enters into play. When M=1.25, the complete theory with a_0=50μm provides distinguishable results from the pure viscoplastic approach (micro-inertia neglected)

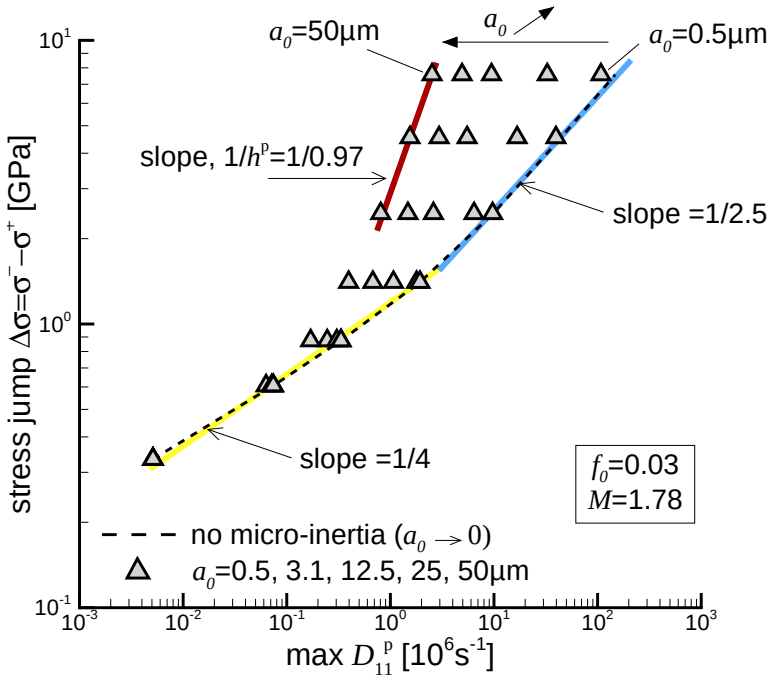

Figure 9: Stress jump across the shock $\Delta\sigma = \sigma^- - \sigma^+$ versus max $\left(D_{11}^p\right)$ in a log-log diagram for f_0=0.03 and various initial void radii (logscale). Also shown for comparison are power-law scaling relationships to the power 0.97 (slope 1/0.97) and 4 (slope 1/4).

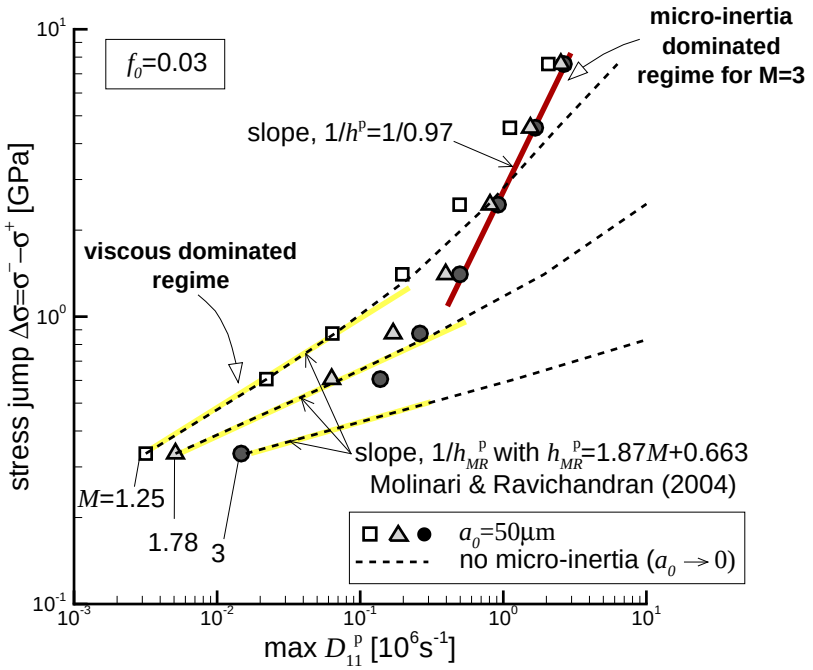

Figure 10: Stress jump across the shock $\Delta\sigma = \sigma^- - \sigma^+$ versus max $\left(D_{11}^{\mathrm{p}}\right)$ in a log-log diagram for f_0=0.03 and various strain rate parameter M. The initial void radius is $50\mu m$. Also shown for comparison are power-law scaling relationships to the power $1/h_{\mathrm{MR}}^{\mathrm{p}}$, where $h_{\mathrm{MR}}^{\mathrm{p}}$ is depending on the strain rate parameter, see Eq. (44)

only when the shock stress is sufficiently large to promote micro-inertia effects. This occurs for σ^-=2GPa ($\Delta\sigma$=1.4GPa). By contrast, when M=3, micro-inertia effects are even noticeable at small σ^-. Fig. 10 also highlights that an exponent $h^{\mathrm{p}} = 1 - f_0$ seems to describe quite well the relationship between the shock stress and the plastic strain rate for $\sigma^- \geq$2.5GPa when M=3. Note that because of reduced micro-inertia effects when M=1.25, the slope $1/(1 - f_0)$ is reached at larger stress level, i.e. when the micro-inertia dominated regime is reached.

This section ends with Fig. 11 showing the stress jump $\Delta\sigma = \sigma^- - \sigma^+$ versus $\max\left(D_{11}^{\mathrm{p}}\right)$ for various initial porosities. Regarding first the pure viscoplastic theory where micro-inertia is neglected (dashed lines), it appears that the slope $1/h_{\mathrm{MR}}^{\mathrm{p}}$ is extending over a larger range of strain rates when the initial porosity is low. Naturally, if $f_0 \to 0$, the material is initially dense and $1/h_{\mathrm{MR}}^{\mathrm{p}}$ would prevail on the entire range of strain rates. Interestingly, it also appears that the slope at larger stress is still 1/2.5, thus being independent of f_0 for values tested here, i.e. $0.03 \leq f_0 \leq 0.3$. For a_0=50μm, micro-inertia effects are more pronounced when f_0 is large. In fact for f_0=0.3, Fig. 11 shows a strong difference between the case where micro-inertia is neglected (small voids) and the case a_0=50μm for which the micro-inertia dominated regime is activated at low stress levels. In addition, it appears that h^{p} is depending on the initial porosity. As it was already mentioned for Fig. 9, $1/h^{\mathrm{p}} = 1/(1 - f_0)$ is shown to be a good estimate of the slope in the log-log diagram of Fig. 11, i.e. $h^{\mathrm{p}} = 1 - f_0$ in the powerlaw relationship (45), when micro-inertia effects are important.

6. Conclusion

Steady plastic shocks propagating in a porous metal have been analyzed. The combined effects of matrix rate sensitivity and micro-inertia have been examined by performing a parametric analysis with porous aluminum as reference material. The relationship between the structure of plastic shocks and material properties (rheological properties of the metal matrix and void configuration) has been uncovered for the simple case of an isotropic distribution of spherical voids with same initial radius. Shocks of relatively small intensity were considered. Therefore, temperature effects could be

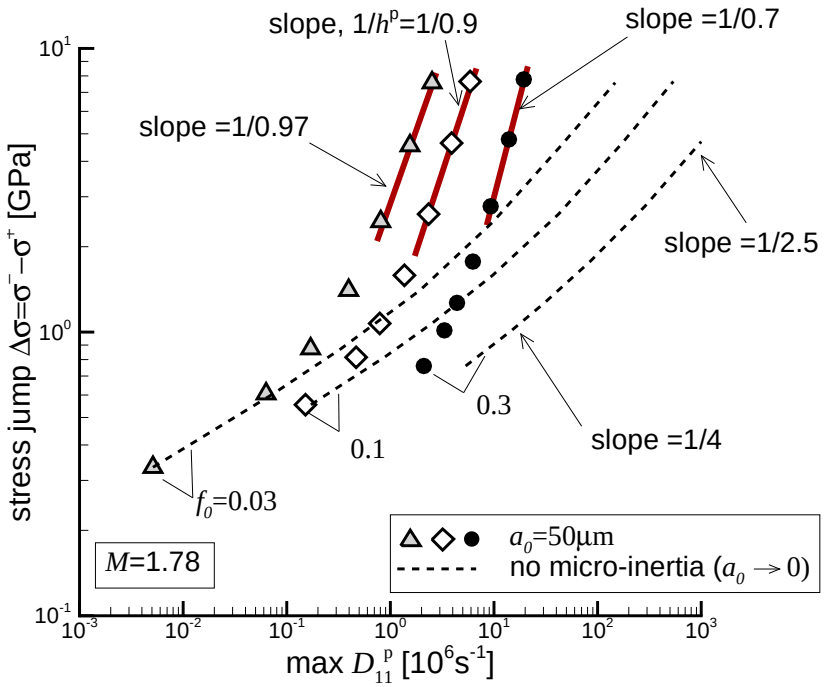

Figure 11: Stress jump across the shock $\Delta\sigma = \sigma^- - \sigma^+$ versus max $\left(D_{11}^{\mathrm{p}}\right)$ in a log-log diagram for various initial porosities. The initial void radius is $50\mu m$ and the strain rate parameter M=1.78. Also shown for comparison are power-law scaling relationships to the power $1/h^{\mathrm{p}}$ with $h^{\mathrm{p}} = 1 - f_0$= 0.97, 0.9, 0.7 for f_0= 0.03, 0.1, 0.3 respectively.

neglected. The modeling is based on the following features: (i) the quasistatic compression curve of the porous medium is analytically characterized from the response of the dense material; (ii) this compression curve is used in place of the Hugoniot to analyze weak shocks; (iii) micro-inertia effects induced by the rapid collapse of voids is accounted for in the modeling of the overall response of the porous medium. These micro-inertia effects are due to the intense acceleration of material particles in the vicinity of collapsing voids.

The class of constitutive laws adopted in our analysis, where the rate sensitivity of matrix material follows a power law formulation, allowed to obtain an interesting insight about how shock structure is modulated by the balance between micro-inertia effects and matrix viscous rate sensitivity.

The following results have been obtained:

- The analysis of the interplay between matrix rate sensitivity and micro-inertia effects has revealed the existence of two extreme regimes governing the structure of plastic shocks which are respectively denoted as viscous dominated regime and micro-inertia dominated regime;

- The viscous dominated regime is prevailing at low shock pressure. In this case the shock structure is mostly affected by the matrix rate sensitivity and by the initial porosity. Micro-inertia effects are negligible and the initial void radius has no effect on results;

- The micro-inertia dominated regime holds at sufficiently large shock pressures. In this case the rate dependency induced by micro-inertia effects overcomes the influence of the matrix rate sensitivity. The shock layer width is scaled by the initial void radius. The rate sensitivity of the matrix material has a minor effect on the shock structure;

- The transition between the viscous and micro-inertia dominated regimes is modulated by the void radius. Thus, for an intermediate range of shock pressures, the shock layer is structured by the combined effects of matrix rate sensitivity and rate effects due to microscale inertia. In that regime, the shock layer width can

be additively decomposed in two contributions (respectively viscous and micro-inertia controlled), thus reflecting in a clear manner the involvement of the two effects;

- The way strain localization is taking place within the shock structure has been uncovered from the examination of the strain rate distribution. Firstly, the strain rate profile for porous metals appears to be highly asymmetric as compared to dense metals. This is due to the succession of two compression processes, the collapse of voids being followed by the compression of the densified material. These distinct compression processes can lead (when micro-inertia effects are negligible) to the existence of two distinct peaks in the strain-rate profile;

- The Swegle and Grady power law (relating the variation of stress across the shock to the maximum strain rate within the shock) which was previously established for dense metals is shown here to have a completely different form for porous metals as an aftermath of porosity and micro-inertia effects. For dense metals, the Swegle and Grady law takes the form: $\max\left(D_{11}^{\mathrm{p}}\right) = H\Delta\sigma^{h^{\mathrm{p}}}$ with $h^{\mathrm{p}} = 4$. For a porous metal, it is found that results cannot be represented by a single power law. Instead, the imprints of the viscous and micro-inertia regimes can be found on the $\Delta\sigma$-$\max\left(D_{11}^{\mathrm{p}}\right)$ relationship. At low shock pressure (viscous dominated regime) the Swegle and Grady law is recovered with an exponent for porous aluminum close to $h^{\mathrm{p}} = 1.87M + 0.663$ when the porosity is not too large. This exponent is function of the matrix rate sensitivity $m = 1/M$. On the other hand, for sufficiently large shock pressures (micro-inertia dominated regime) another form of the Swegle and Grady law is found with an exponent h^{p} depending on the void configuration (initial porosity) but independent of the matrix rate sensitivity.

- It has been shown that for porous aluminum with initial porosity f_0, the exponent of the Swegle and Grady law at large pressure (micro-inertia dominated regime) is given by $h^{\mathrm{p}} = 1 - f_0$ in the range explored here, $0.03 \leq f_0 \leq 0.3$. Thus, h^{p} can be as small as 0.7 for shock pressures larger than 5GPa. This small value of

h^p is quite beneficial since it is conducive to a shock mitigation by attenuating the level of strain rate and of acceleration sustained by material particles.

The analysis developed in this paper furnishes a fundamental tool to design the internal structure of a porous material in order to mitigate the shock severity. Clearly, by spreading the shock layer width, one is able to lower the extreme accelerations sustained by material particles and consequently to significantly attenuate some of the negative effects resulting from a high energy impact. Our results may help designers of shock wave mitigation devices to tailor the shock layer width in order to prevent instructures passengers or equipments from strong accelerations. This can be envisioned with the development of additive manufacturing which could provide more dedicated and controlled microstructures following, for instance, a specific pore size and geometry for a given porosity. Further development of the model would be to account for non-spherical voids, Sartori et al. (2015).

Aknowledgment

The authors gratefully acknowledge the financial support of the French National Research Agency ANR (LabEx DAMAS, 535 Grant No. ANR-11-LABX-0008-01).

Appendix A. Relationship between shock speed C and particle velocity v^-

In this section, we propose to complement the numerical solving used in Czarnota et al. (2017) by an approximate analytical solution. The present approach reveals the same predictive capabilities as the numerical approach.

The analytical relation is derived for relatively large stress amplitudes $\sigma^- = -T_1^-$ so that the porous material of initial porosity f_0 is fully densified before reaching σ^- on the quasistatic compression curve. Moreover, it is also assumed that under such shock amplitudes, states (+) and (e) nearly coincide, see Fig. 2, so that $-T_1^+ \simeq \sigma^{\rm e}$, $\lambda_1^+ \simeq \lambda_1^{\rm e}$, $v^+ \simeq v^{\rm e}$. From Eqs (34-35), the plastic shock velocity is then expressed as:

$$C = \sqrt{\frac{\sigma^- - \sigma^{\rm e}}{\rho_{0\rm m}\,(1-f_0)\,\left(\lambda_1^{\rm e} - \lambda_1^-\right)}}\,, \tag{A.1}$$

and the particle velocity v^- is given by:

$$v^- = v^{\rm e} + C\left(\lambda_1^{\rm e} - \lambda_1^-\right)\,. \tag{A.2}$$

The particle velocity $v^{\rm e}$ is linked to the elastic stretch $\lambda_1^{\rm e}$ and the elastic limit $\sigma^{\rm e}$ according to Eqs (39-40):

$$v^{\rm e} = (1-\lambda_1^{\rm e})\sqrt{\frac{\sigma^{\rm e}}{\rho_{0\rm m}\,(1-f_0)\,(1-\lambda_1^{\rm e})}}\,. \tag{A.3}$$

The two quantities $\lambda_1^{\rm e}$ and $\sigma^{\rm e}$ are needed to evaluate C and v^- from respectively Eq. (A.1) and Eqs (A.2-A.3). Note that so far, the total stretch λ_1^- is unknown and needs to be identified in terms of σ^-. In so doing, a parametric representation $(C(\sigma^-),\, v^-(\sigma^-))$ of the $C - v^-$ curve will be obtained with Eqs (A.1-A.2). This aspect is addressed in the following.

Fig. A.12 displays quasistatic compression curves for dense and porous aluminum, but here σ is represented in terms of the specific volume $\frac{\lambda_1}{\rho_{0\rm m}(1-f_0)}$ (for porous) and $\frac{\lambda_{1\rm d}}{\rho_{0\rm m}}$ (for dense), while before, in Fig. 2, we considered σ vs λ_1. Fig. A.12 shows that the porous material response coincides with that of the dense material as soon as full densification is achieved. Therefore, with good accuracy, we have:

$$\frac{\lambda_{1\rm d}^-}{\rho_{0\rm m}} = \frac{\lambda_1^-}{\rho_{0\rm m}(1-f_0)}\,. \tag{A.4}$$

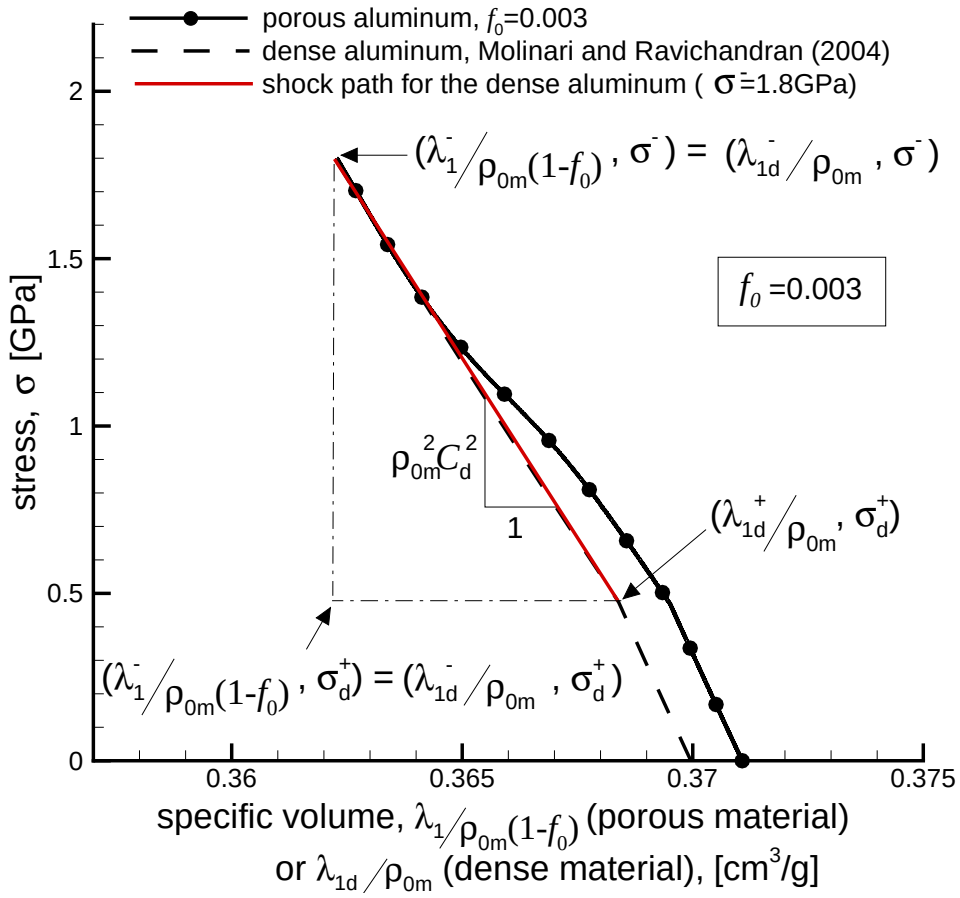

Figure A.12: Quasistatic compression curves for porous (initial porosity f_0=0.003) and dense materials in respectively the $(\frac{\lambda_1}{\rho_{0m}(1-f_0)}, \sigma)$ and the $(\frac{\lambda_{1d}}{\rho_{0m}}, \sigma)$ diagrams where λ_1 and λ_{1d} refer respectively to the stretch in the porous and dense materials. Once the porous medium is fully densified, the path is almost collinear to the dense material response up to σ^-.

The merging of the curves in Fig. A.12 when σ is large enough can be interpreted as follows. Consider a unit mass of porous material. The initial volume of porous material is given by:

$$\frac{1}{\rho_{0\mathrm{m}}\,(1-f_0)} = V_0 = V_{0\mathrm{m}} + V_{0\mathrm{v}} \tag{A.5}$$

where the initial matrix volume and void-phase volume are respectively denoted by $V_{0\mathrm{m}}$ and $V_{0\mathrm{v}}$. Note that the mass is solely due to the matrix:

$$\rho_{0\mathrm{m}} V_{0\mathrm{m}} = 1\,. \tag{A.6}$$

When σ is large enough, voids are closed in the porous material (void volume $V_{\mathrm{v}} = 0$), and the matrix volume V_{m} is equal to the total volume $V = V_{\mathrm{m}}$. The longitudinal stretch is $\lambda_1 = \frac{V}{V_0}$ and we have: $\lambda_1 = \frac{V_{\mathrm{m}}}{V_{0\mathrm{m}}+V_{0\mathrm{v}}} = \frac{V_{\mathrm{m}}}{V_{0\mathrm{m}}}\frac{V_{0\mathrm{m}}}{V_{0\mathrm{m}}+V_{0\mathrm{v}}}$ and finally:

$$\lambda_1 = \frac{V_{\mathrm{m}}}{V_{0\mathrm{m}}}\,(1-f_0) \tag{A.7}$$

Consider now a unit mass of virgin dense material. The initial volume is $\frac{1}{\rho_{0\mathrm{m}}}$, identical to the initial matrix volume of the porous material of unit mass, see Eq. (A.6). This dense material is subjected to uniaxial compression up to the same stress level σ. We denote by $V_{\mathrm{m}}^{\mathrm{dense}}$ the final volume (the subscript $(\cdot)_{\mathrm{m}}$ refers to the fact that the initial volume is $V_{0\mathrm{m}}$). Thus, the longitudinal stretch of the dense material is given by:

$$\lambda_{1\mathrm{d}} = \frac{V_{\mathrm{m}}^{\mathrm{dense}}}{V_{0\mathrm{m}}} \tag{A.8}$$

Note that V_{m} and $V_{\mathrm{m}}^{\mathrm{dense}}$ are obtained from same initial volumes, $V_{0\mathrm{m}}$, and same stress level σ. However, even when voids are closed, V_{m} and $V_{\mathrm{m}}^{\mathrm{dense}}$ should be a priori slightly different since the loading histories are not the same. Indeed, due to void closure, the matrix material sustains larger plastic deformations as compared to the initially dense material. Plastic deformations are volume preserving, but the level of work-hardening is affected and has some influence on material responses. Nevertheless, it appears from Fig. A.12 that $V_{\mathrm{m}} \simeq V_{\mathrm{m}}^{\mathrm{dense}}$ when σ is sufficiently large, so that the early difference in work-hardening is getting weaker. The result $V_{\mathrm{m}} \simeq V_{\mathrm{m}}^{\mathrm{dense}}$comes from Eq. (A.4) which reads $\frac{\lambda_1}{1-f_0} = \lambda_{1\mathrm{d}}$ and from Eqs (A.7-A.8). In the following, the subscript 'd' refers to dense material properties, or to shock experiments in dense

material. From compression curves shown in Fig. A.12, one can deduce the total stretch λ_1^- corresponding to σ^-.

Considering now the Rayleigh line defined for the dense material as:

$$\sigma^- - \sigma_{\rm d}^+ = \rho_{0\rm m} C_{\rm d}^2 \left(\lambda_{1\rm d}^+ - \lambda_{1\rm d}^-\right) , \tag{A.9}$$

the following relationship is obtained by using Eq. (A.4):

$$\lambda_1^- = (1-f_0)\left(\lambda_{1\rm d}^+ - \frac{\sigma^- - \sigma_{\rm d}^+}{\rho_{0\rm m} C_{\rm d}^2}\right) . \tag{A.10}$$

In Eqs (A.9-A.10), $C_{\rm d}$ stands for the plastic shock velocity of the initially dense material under shock stress σ^-. $\lambda_{1\rm d}^+$ and $\sigma_{\rm d}^+$ correspond to stretch and stress at the elastic limit of the initially dense material.

A linear dependence of $C_{\rm d}$ to the shock particle velocity $v_{\rm d}^-$ has been obtained by Swegle & Grady (1985) for numerous dense materials (e.g. beryllium, iron, copper, aluminum,...). Such a relationship is also retrieved by the modeling proposed by Molinari & Ravichandran (2004) which reads:

$$C_{\rm d} = C_{\rm d}^+ + S(v_{\rm d}^- - v_{\rm d}^+) , \tag{A.11}$$

which is equivalent to know the compression curve for the dense material. $C_{\rm d}^+$ (respectively $v_{\rm d}^+$) is the sound velocity (respectively the particle velocity) associated to the state (+) corresponding to initial yielding. Note that $C_{\rm d}^+$ in Eq. (A.11) is much smaller than the celerity of the elastic precursor $C_{\rm d}^{\rm el}$. The particle velocity $v_{\rm d}^+$ is related to $C_{\rm d}^{\rm el}$ by $v_{\rm d}^+ = C_{\rm d}^{\rm el}(1-\lambda_{1\rm d}^+)$.

For dense materials (f_0=0), Eq. (34) leads to:

$$\sigma^- - \sigma_{\rm d}^+ = \rho_{0\rm m} C_{\rm d} (v_{\rm d}^- - v_{\rm d}^+) . \tag{A.12}$$

A combination of Eqs (A.11) and (A.12) leads to a quadratic equation for the unknown $C_{\rm d}$. The plastic shock velocity in the dense material $C_{\rm d}$ is found:

$$C_{\rm d} = C_{\rm d}(\sigma^-) = \frac{C_{\rm d}^+}{2}\left(1 + \sqrt{1 + \frac{4S\left(\sigma^- - \sigma_{\rm d}^+\right)}{\rho_{0\rm m}\left(C_{\rm d}^+\right)^2}}\right) . \tag{A.13}$$

The stretch λ_1^- corresponding to the stress σ^- can now be determined from Eq. (A.10) with C_d given by Eq. (A.13) so that:

$$\lambda_1^- = \lambda_1^-(\sigma^-) = (1-f_0)\left(\lambda_{1\mathrm{d}}^+ - \frac{\sigma^- - \sigma_\mathrm{d}^+}{\rho_{0\mathrm{m}}\left(C_\mathrm{d}(\sigma^-)\right)^2}\right) . \tag{A.14}$$

Then the shock speed C is obtained in terms of σ^- with Eq. (A.1):

$$C = C(\sigma^-) = \sqrt{\frac{\sigma^- - \sigma^\mathrm{e}}{\rho_{0\mathrm{m}}\left(1-f_0\right)\left(\lambda_1^\mathrm{e} - \lambda_1^-(\sigma^-)\right)}} , \tag{A.15}$$

and v^- is obtained from Eq. (A.2):

$$v^- = v^-(\sigma^-) = v^\mathrm{e} + C\left(\lambda_1^\mathrm{e} - \lambda_1^-(\sigma^-)\right) . \tag{A.16}$$

With Eqs (A.15-A.16), we have a parametric representation of the curve C vs v^- in terms of the parameter σ^-.

Comparisons are now made between the analytical approach presented above and the numerical solving used in Czarnota et al. (2017) which is denoted below as reference solution. Material parameters for porous aluminum are listed in Table 1. The values of C_d^+, v^+, $\lambda_{1\mathrm{d}}^+$ and σ_d^+ for dense aluminum are taken from Molinari & Ravichandran (2004): $C_\mathrm{d}^+ = 5320$m/s, v^+=27m/s, $\lambda_{1\mathrm{d}}^+$=0.99578 and σ_d^+=0.473GPa. For the parameter S in Eq. (A.11), these authors predicted, for moderate shocks ($\sigma^- \leq 9$GPa), the value S=1.347 (close to $S = 1.337$ obtained by Swegle & Grady, 1985).

Fig. A.13-a shows the shock speed C in terms of the particle velocity v^- for various initial porosities. The analytical parametric solution is displayed for S=1.347, and appears to match well the reference solution except for small values of σ^-. For lower stresses, differences are naturally observed since the densification is not complete and the approximation made in this section is no more valid.

Fig. A.13-a also reveals some discrepancies at large shock amplitudes. This is observed for materials with low porosity and shock stresses greater than 30GPa. The observed difference is the consequence of the adopted value of S which can be adjusted to reproduce the dense response provided by the model up to large shock amplitudes. From Fig. A.13-b, a better agreement between the reference solution and the analytical approach is obtained with S=1.2. With this value of S, the analytical solution provides

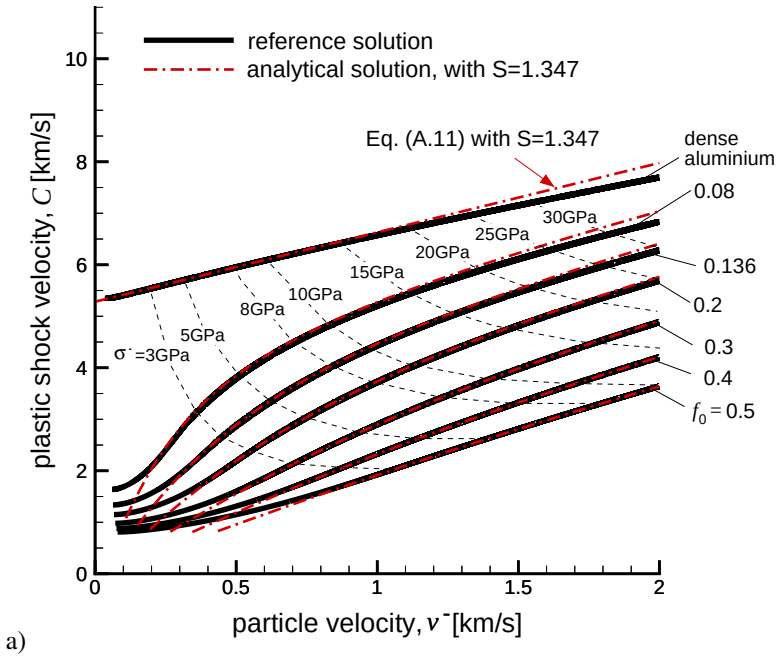

a)

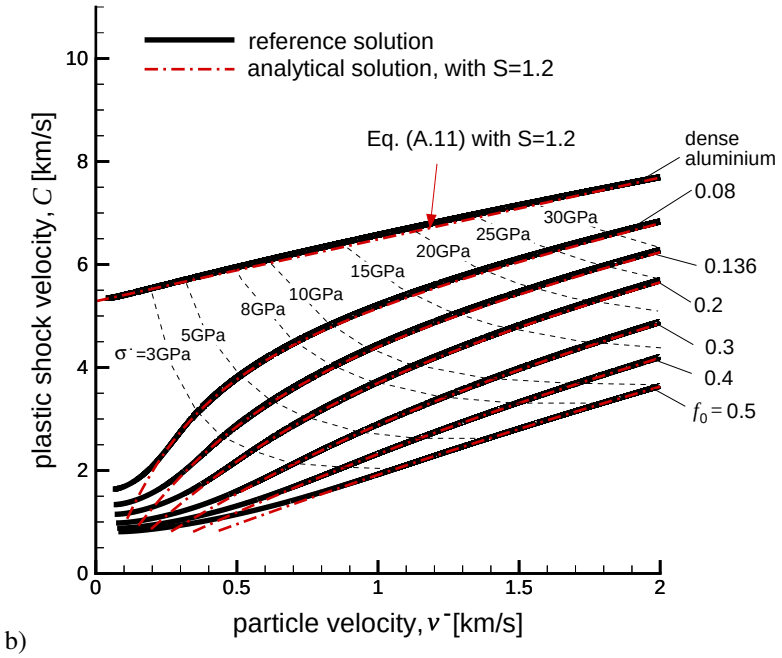

b)

Figure A.13: Comparison of C-v^- curves obtained from the reference solution (see Czarnota et al., 2017) and that obtained from the analytical approach of section Appendix A with a) $S = 1.347$ corresponding to value determined in Molinari & Ravichandran (2004) b) $S = 1.2$ deduced from a fit of the dense curve.

an excellent match with the reference solution when the material is fully densified at the rear of the shock. It should be noted that the reference solution reproduces closely experimental data up to σ^{-}=30GPa for aluminum alloys in a large range of porosities, see Fig. 4 in Czarnota et al. (2017). As a consequence, the analytical method shows the same predictive capabilities having great advantages as regards implementation.

Appendix B. Shock structure problem: solving steps

The shock structure is analyzed for a given shock intensity which is characterized either by the shock speed C or equivalently by the stress σ^-. It is reminded that (λ_1^-, σ^-) is defined as the intersection of the Rayleigh line with the quasistatic compression curve $\mathscr{C}_{\rm Y}$.

The shock-structure is displayed in terms of the position ξ, with $\xi = +\infty$ and $\xi = -\infty$ being respectively ahead and behind the shock layer.

Appendix B.1. Shock structure when disregarding micro-inertia

When micro-inertia is neglected, the system of equations is deduced from Eqs (28) and (25-26), which, by considering $\xi = X - Ct$, reduces to the following set of nonlinear equations:

$$\begin{cases} \gamma^{\rm p}_{,\xi} = -\dfrac{\Phi}{C}\,, & \text{(B.1a)} \\ \lambda^{\rm p}_{1,\xi} = \dfrac{\lambda^{\rm p}_1 (1-f)\,\Phi \left[\frac{2\Sigma_{\rm eq}}{\bar\sigma} + q_1 q_2 f \sinh\left(-\frac{3}{2} q_2 \frac{\Sigma_{\rm m}}{\bar\sigma}\right)\right]}{3C\left[\left(\frac{\Sigma_{\rm eq}}{\bar\sigma}\right)^2 + \frac{3\Sigma_{\rm m}}{2\bar\sigma} q_1 q_2 f \sinh\left(\frac{3}{2} q_2 \frac{\Sigma_{\rm m}}{\bar\sigma}\right)\right]}\,, & \text{(B.1b)} \\ f_{,\xi} = \dfrac{(1-f)^2\,\Phi q_1 q_2 f \sinh\left(-\frac{3}{2} q_2 \frac{\Sigma_{\rm m}}{\bar\sigma}\right)}{C\left[\left(\frac{\Sigma_{\rm eq}}{\bar\sigma}\right)^2 + \frac{3\Sigma_{\rm m}}{2\bar\sigma} q_1 q_2 f \sinh\left(\frac{3}{2} q_2 \frac{\Sigma_{\rm m}}{\bar\sigma}\right)\right]}\,. & \text{(B.1c)} \end{cases}$$

At $\xi = +\infty$ we have state (+), therefore:

$$f\,(\xi = +\infty) = f^+,\ \lambda^{\rm p}_1\,(\xi = +\infty) = \lambda^{\rm p+}_1,\ \gamma^{\rm p}\,(\xi = +\infty) = \gamma^{\rm p+}. \qquad \text{(B.2)}$$

Since viscous effects are neglected along the early compression stage (fan from state (e) to state (+)), we have $\Phi(\xi = +\infty)$=0 (zero overstress).

To solve the differential system (B.1) we consider an arbitrary position $\xi_{\rm (init)}$ where initial conditions are those of state (+) slightly perturbed. Specifically, the initial plastic stretch and porosity are taken as $\lambda^{\rm p}_{1\rm (init)} = \lambda^{\rm p+}_1$ and $f_{\rm (init)} = f^+$ while the initial plastic shear strain is taken as $\gamma^{\rm p}_{\rm (init)} = \gamma^{\rm p+} - \delta\gamma^{\rm p}$ with $\delta\gamma^{\rm p} = 10^{-5}$.

The initial total stretch $\lambda_{1\rm (init)}$ and $T_{1\rm (init)}(= -\sigma_{\rm (init)})$ are computed by using Eqs (13a, 14) and (36) with $f = f_{\rm (init)} = f^+$ and $\lambda^{\rm p}_1 = \lambda^{\rm p}_{1\rm (init)} = \lambda^{\rm p+}_1$. Thus, $T_{1\rm (init)} = T^+_1$ and

$\lambda_{1(\text{init})} = \lambda_1^+$. $T_{2(\text{init})}$ is obtained from Eq. (13b) so that the Cauchy stress tensor $\boldsymbol{\Sigma}_{(\text{init})}$ can determined from Eq. (12). The two invariants $\Sigma_{\text{m(init)}}$ and $\Sigma_{\text{eq(init)}}$ can then be calculated from the definition $\Sigma_{\text{m(init)}} = 1/3\text{tr}(\boldsymbol{\Sigma}_{(\text{init})})$ and $\Sigma_{\text{eq(init)}} = \sqrt{\frac{3}{2}\boldsymbol{\Sigma}_{(\text{init})}' : \boldsymbol{\Sigma}_{(\text{init})}'}$, $\boldsymbol{\Sigma}_{(\text{init})}'$ being the deviatoric part of $\boldsymbol{\Sigma}_{(\text{init})}$. The matrix flow stress $\bar{\sigma}_{(\text{init})}$ is next deduced from the GTN yield viscoplastic flow surface (22). The rate-independent strength $\bar{\sigma}_{a(\text{init})}$ of the matrix material is calculated using Eq.(29) with the perturbed $\gamma^{\text{p}} = \gamma^{\text{p}}_{(\text{init})} = \gamma^{\text{p}+} - \delta\gamma^{\text{p}}$. This implies an initial positive overstress $\bar{\sigma}_{(\text{init})} - \bar{\sigma}_{a(\text{init})}$ which in turns leads to a non-zero $\Phi_{(\text{init})}$, see Eqs.(27-28). It has been checked that lower values of $\delta\gamma^{\text{p}}$ conduct to identical results modulo a shift of the shock profile along the ξ-axis.

Let us now note $\lambda_1^{\text{p}}(\xi)$, $\gamma^{\text{p}}(\xi)$ and $f(\xi)$ known values of λ_1^{p}, γ^{p} and f at position $\xi < \xi_{(\text{init})}$. Using Eqs (B.1), one has to update all mechanical fields at position $\xi + d\xi$ (with $d\xi < 0$). This is done as follows. First, one has to to determine all quantities involved in the right hand side of Eqs (B.1a)-(B.1c) at position ξ :

1. the matrix strength $\bar{\sigma}_a(\xi)$ is deduced from Eq. (29);
2. besides, $\lambda_1(\xi)$ and $T_1(\xi)$ are jointly found by using Eqs (13a-14) and Eq. (36);
3. $T_2(\xi)$ is next obtained from Eq. (13b) and Cauchy stress invariants $\Sigma_{\text{m}}(\xi)$, $\Sigma_{\text{eq}}(\xi)$ can thus be deduced;
4. The GTN viscoplastic flow surface (22), $\Omega\left(\boldsymbol{\Sigma}, \bar{\sigma}, f\right) = 0$, is then used to compute $\bar{\sigma}(\xi)$;
5. The overstress $F_\sigma(\xi) = \bar{\sigma}(\xi) - \sigma_a(\xi)$ can now be evaluated;
6. $\Phi(\xi)$ is subsequently obtained from Eq. (27).

From the foregoing, the right hand side of Eqs (B.1) can be evaluated at ξ. Based on a 4th order Runge Kutta scheme, the three quantities : $\lambda_1^{\text{p}}(\xi + d\xi)$, $\gamma^{\text{p}}(\xi + d\xi)$ and $f(\xi + d\xi)$ are obtained. The process is continued until $\frac{d\lambda_1^{\text{p}}}{d\xi}$ is of negligible magnitude.

Appendix B.2. Shock structure with micro-inertia effects

When micro inertia is accounted for, Eqs (20, 28, 25) are used. For the purpose of solving the complete set of governing equations, Eq. (20) is rewritten in terms of the current porosity. Owing to matrix incompressibility, the current void radius a is expressed in terms of initial and current porosities, respectively f_0 and f, and initial void size a_0:

$$a = a_0 \left(\frac{1-f_0}{f_0}\right)^{1/3} \left(\frac{f}{1-f}\right)^{1/3} . \tag{B.3}$$

Using Eqs (6) and (B.3), Eq. (20) thus becomes:

$$\Sigma_{\rm m} = \Sigma^\star_{\rm m} + \frac{\rho_{0\rm m} a_0^2}{3} \left(\frac{1-f_0}{f_0}\right)^{2/3} \left[\frac{f^{-1/3}-1}{(1-f)^{5/3}}\ddot{f} + \frac{-\frac{1}{6}f^{-4/3} + 2f^{-1/3} - \frac{11}{6}}{(1-f)^{8/3}}\dot{f}^2\right] . \tag{B.4}$$

The system of equations formed with Eqs (28, 25, B.4) leads to the following set of ODEs:

$$\begin{cases} \gamma^{\rm p}_{,\xi} = -\dfrac{\Phi}{C} , & \text{(B.5a)} \\ \lambda^{\rm p}_{1,\xi} = \dfrac{\lambda^{\rm p}_1 (1-f)\,\Phi\left[\frac{2\Sigma_{\rm eq}}{\bar\sigma} + q_1 q_2 f \sinh\left(-\frac{3}{2} q_2 \frac{\Sigma^\star_{\rm m}}{\bar\sigma}\right)\right]}{3C\left[\left(\frac{\Sigma_{\rm eq}}{\bar\sigma}\right)^2 + \frac{3\Sigma^\star_{\rm m}}{2\bar\sigma} q_1 q_2 f \sinh\left(\frac{3}{2} q_2 \frac{\Sigma^\star_{\rm m}}{\bar\sigma}\right)\right]} , & \text{(B.5b)} \\ f_{,\xi} = \hat{f} , & \text{(B.5c)} \\ \hat{f}_{,\xi} = \dfrac{3\left(\Sigma_{\rm m} - \Sigma^\star_{\rm m}\right)}{\rho_{0\rm m} a_0^2 C^2 \left(\frac{1-f_0}{f_0}\right)^{2/3}} (1-f)^{5/3} \left(f^{-1/3}-1\right)^{-1} \\ \quad - \hat{f}^2 (1-f)^{-1} \left(f^{-1/3}-1\right)^{-1} \left(2f^{-1/3} - \dfrac{1}{6} f^{-4/3} - \dfrac{11}{6}\right) . & \text{(B.5d)} \end{cases}$$

where a new variable is introduced: $\hat{f} = f_{,\xi}$.

According to Eq. (26), and using $\Sigma^\star_{\rm eq} = \Sigma_{\rm eq}$, we have:

$$\hat{f} = \frac{(1-f)^2\,\Phi(\gamma^{\rm p}, \bar\sigma) q_1 q_2 f \sinh\left(-\frac{3}{2} q_2 \frac{\Sigma^\star_{\rm m}}{\bar\sigma}\right)}{C\left[\left(\frac{\Sigma_{\rm eq}}{\bar\sigma}\right)^2 + \frac{3\Sigma^\star_{\rm m}}{2\bar\sigma} q_1 q_2 f \sinh\left(\frac{3}{2} q_2 \frac{\Sigma^\star_{\rm m}}{\bar\sigma}\right)\right]} . \tag{B.6}$$

To make apparent the dependence of the right hand side of the differential system (B.5) upon the main variables $\gamma^{\rm p}$, $\lambda^{\rm p}_1$, f and $\hat{f}$, one may implicitly solve Eq. (B.6) in terms of $\frac{\Sigma^\star_{\rm m}}{\bar\sigma}$:

$$\Sigma^\star_{\rm m} = \bar\sigma K\left(f, \hat{f}, \Phi(\gamma^{\rm p}, \bar\sigma), \frac{\Sigma_{\rm eq}}{\bar\sigma}\right) \tag{B.7}$$

and substitute this expression of $\Sigma_{\mathrm{m}}^{\star}$ into Eq. (B.5b) and Eq. (B.5d).

The initial conditions in terms of λ_1^{p}, γ_{p}, f and $\hat{f}$ are needed. Firstly, few steps of integration are calculated by adopting the micro-inertia independent formalism described in Appendix B.1. Thus, near state (+) where the shock profile is initiated, voids are almost unchanged and micro-inertia effects are negligible. As a consequence, the term $\hat{f}$ is evaluated first from Eq. (26) using $\Sigma_{\mathrm{eq}}^{\star} = \Sigma_{\mathrm{eq}}$ (see also Eq. B.1c):

$$\hat{f} = \frac{(1-f)^2\,\Phi q_1 q_2 f \sinh\left(-\frac{3}{2}q_2\frac{\Sigma_{\mathrm{m}}}{\bar{\sigma}}\right)}{C\left[\left(\frac{\Sigma_{\mathrm{eq}}}{\bar{\sigma}}\right)^2 + \frac{3\Sigma_{\mathrm{m}}}{2\bar{\sigma}} q_1 q_2 f \sinh\left(\frac{3}{2}q_2\frac{\Sigma_{\mathrm{m}}}{\bar{\sigma}}\right)\right]}\,. \tag{B.8}$$

Let us note $\lambda_1^{\mathrm{p}}(\xi)$, $\gamma^{\mathrm{p}}(\xi)$ $f(\xi)$ and $\hat{f}(\xi)$ known values of λ_1^{p}, γ^{p}, f and $\hat{f}$ at position ξ. The solution at $\xi + d\xi$ can be obtained following mainly the same procedure as in the problem without micro inertia (see Appendix B.1). The only difference emerges from the occurrence of the additional unknown $\Sigma_{\mathrm{m}}^{\star}$. The first three steps are identical so $N(\xi)$, $\bar{\sigma}_a(\xi)$, $\lambda_1(\xi)$, $T_1(\xi)$, $T_2(\xi)$, $\Sigma_{\mathrm{m}}(\xi)$ and $\Sigma_{\mathrm{eq}}(\xi)$ are also known. Subsequent steps are described in the following :

4*. The GTN viscoplastic flow surface (22) is used for the quasistatic stress $\boldsymbol{\Sigma}^{\star}$, $\Omega\left(\boldsymbol{\Sigma}^{\star}, \bar{\sigma}, f\right) = 0$. Thus, the ratio $\frac{3}{2}q_2\frac{\Sigma_{\mathrm{m}}^{\star}(\xi)}{2\bar{\sigma}(\xi)}$ can be expressed as a function of the ratio $\frac{\Sigma_{\mathrm{eq}}^{\star}(\xi)}{\bar{\sigma}(\xi)} = \frac{\Sigma_{\mathrm{eq}}(\xi)}{\bar{\sigma}(\xi)}$:

$$\frac{3}{2}q_2\frac{\Sigma_{\mathrm{m}}^{\star}(\xi)}{2\bar{\sigma}(\xi)} = -\zeta\,\mathrm{arccosh}\left\{\frac{1}{2q_1 f(\xi)}\left[1 + (q_1 f(\xi))^2 - \left(\frac{\Sigma_{\mathrm{eq}}(\xi)}{\bar{\sigma}(\xi)}\right)^2\right]\right\} \tag{B.9}$$

where $\zeta = \hat{f}(\xi)/|\hat{f}(\xi)|$ is the sign of $f_{,\xi}$.

5*. Using Eq. (B.9) to substitute $\frac{3}{2}q_2\frac{\Sigma_{\mathrm{m}}^{\star}(\xi)}{2\bar{\sigma}(\xi)}$ into Eq. (B.6) and reminding that $\Sigma_{\mathrm{eq}}(\xi)$ is known, one can compute $\bar{\sigma}(\xi)$;

6*. Lastly, $\Phi(\xi)$ is determined and $\Sigma_{\mathrm{m}}^{\star}(\xi)$ is given by Eq. (B.9);

7*. The right hand side of Eqs (B.5) is thus determined and γ^{p}, λ_1^{p}, f and $\hat{f}$ can be incremented.

It is worth noticing that the problem without micro-inertia effects is retrieved by setting $\rho_{0\mathrm{m}} = 0$ in Eq. (B.5d). Then, we have $\Sigma_{\mathrm{m}} = \Sigma_{\mathrm{m}}^{\star} = \bar{\sigma}K(f, \hat{f}, \Phi, \frac{\Sigma_{\mathrm{eq}}}{\bar{\sigma}})$ which is equivalent to Eq. (B.6) and the differential system (B.1) is obtained.

References

Austin, R. A., & McDowell, D. L. (2011). A dislocation-based constitutive model for viscoplastic deformation of fcc metals at very high strain rates. *Int. J. Plast.*, *27*, 1 – 24.

Austin, R. A., & McDowell, D. L. (2012). Parameterization of a rate-dependent model of shock-induced plasticity for copper, nickel, and aluminum. *Int. J. Plast.*, *32-33*, 134 – 154.

Barthélémy, R., Jacques, N., Kerampran, S., & Vermeersch, F. (2016). Modelling of micro-inertia effects in closed-cell foams with application to acoustic and shock wave propagation. *Int. J. Solids Struct.*, *97-98*, 445–457.

Butcher, B. M., Carroll, M. M., & Holt, A. C. (1974). Shock-wave compaction of porous aluminum. *J. Appl. Phys.*, *45*, 3864–3875.

Carroll, M. M., & Holt, A. C. (1972). Static and dynamic pore collapse relations for ductile porous materials. *J. Appl. Phys.*, *43*, 1626–1636.

Carroll, M. M., Kim, K. T., & Nesterenko, V. F. (1986). The effect of temperature on viscoplastic pore collapse. *J. Appl. Phys.*, *59*, 1962–1967.

Clifton, R. J. (1970). On the analysis of elastic/visco-plastic waves of finite uniaxial strain. In J. J. Burke, & V. Weiss (Eds.), *Shock Waves and the Mechanical Properties of Solids* (pp. 73–116). Syracuse University Press.

Cortés, R. (1992). The growth of microvoids under intense dynamic loading. *Int. J. Solids Struct.*, *29*, 1339–1350.

Czarnota, C., Jacques, N., Mercier, S., & Molinari, A. (2008). Modelling of dynamic ductile fracture and application to the simulation of plate impact tests on tantalum. *J. Mech. Phys. Solids*, *56*, 1624–1650.

Czarnota, C., Mercier, S., & Molinari, A. (2006). Modelling of nucleation and void growth in dynamic pressure loading, application to spall test on tantalum. *Int. J. Fract.*, *141*, 177–194.

Czarnota, C., Molinari, A., & Mercier, S. (2017). The structure of steady shock waves in porous metals. *J. Mech. Phys. Solids*, *107*, 204 – 228.

Ding, J., & Asay, J. (2009). Numerical study of rate-dependent strength behavior under ramp and shock wave loading. *Int. J. Plast.*, *25*, 695 – 714. Special Issue In Honor of Dattatraya (Datta) Dandekar.

Dunin, S. Z., & Surkov, V. V. (1979). Structure of a shock wave front in a porous solid. *J. Appl. Mech. Tech. Phys.*, *20*, 612–618.

Franco Navarro, P., Benson, D. J., & Nesterenko, V. F. (2016). Multiple scales of shock waves in dissipative laminate materials. *Phys. Rev. E*, *94*, 033002.

Grady, D. E. (2010). Structured shock waves and the fourth-power law. *J. Appl. Phys.*, *107*, 013506.

Gurson, A. L. (1977). Continuum theory of ductile rupture by void nucleation and growth : Part I - yield criteria and flow rules for porous ductile media. *J. Eng. Mater. Technol.*, *99*, 2–15.

Jacques, N., & Barthélémy, R. (2018). An analytical expression for the hugoniot stressstrain curve of elastic-plastic cellular materials. *Int. J. Impact Eng.*, *115*, 76 – 80.

Jacques, N., Czarnota, C., Mercier, S., & Molinari, A. (2010). A micromechanical constitutive model for dynamic damage and fracture of ductile materials. *Int. J. Fract.*, *162*, 159–175.

Johnson, J. N. (1981). Dynamic fracture and spallation in ductile solids. *J. Appl. Phys.*, *52*, 2812–2825.

Johnson, J. N., & Barker, L. M. (1969). Dislocation dynamics and steady plastic wave profiles in 6061-T6 Aluminum. *J. Appl. Phys.*, *40*, 4321–4334.

Kitagawa, K., Yamashita, S., Takayama, K., & Yasuhara, M. (2009). Attenuation properties of blast wave through porous layer. In K. Hannemann, & F. Seiler (Eds.), *Shock Waves* (pp. 73–78). Berlin, Heidelberg: Springer Berlin Heidelberg.

Knowles, J. K. (2002). Impact-induced tensile waves in a rubberlike material. *J. Appl. Math.*, *62*, 1153–1175.

Krasnikov, V., & Mayer, A. (2015). Plasticity driven growth of nanovoids and strength of aluminum at high rate tension: Molecular dynamics simulations and continuum modeling. *Int. J. Plast.*, *74*, 75 – 91.

Lloyd, J. T., Clayton, J. D., Austin, R. A., & McDowell, D. L. (2015). Shock compression modeling of metallic single crystals: comparison of finite difference, steady wave, and analytical solutions. *Adv. Model. and Simul. in Eng. Sci.*, *2*, 1–19.

Mayer, A. E., Ebel, A. A., & Al-Sandoqachi, M. K. (2020). Plastic deformation at dynamic compaction of aluminum nanopowder: Molecular dynamics simulations and mechanical model. *Int. J. Plast.*, *124*, 22 – 41.

Molinari, A., & Daraio, C. (2009). Stationary shocks in periodic highly nonlinear granular chains. *Phys. Rev. E*, *80*, 056602.

Molinari, A., & Mercier, S. (2001). Micromechanical modelling of porous materials under dynamic loading. *J. Mech. Phys. Solids*, *49*, 1497–1516.

Molinari, A., & Ravichandran, G. (2004). Fundamental structure of steady plastic shock waves in metals. *J. Appl. Phys.*, *95*, 1718 – 1732.

Molinari, A., & Ravichandran, G. (2006). Modeling plastic shocks in periodic laminates with gradient plasticity theories. *J. Mech. Phys. Solids*, *54*, 2495–2526.

Molinari, A., & Wright, T. W. (2005). A physical model for nucleation and early growth of voids in ductile materials under dynamic loading. *J. Mech. Phys. Solids*, *53*, 1476–1504.

Needleman, A., & Tvergaard, V. (1991). An analysis of dynamic, ductile crack growth in a double edge cracked specimen. *Int. J. Fract.*, *49*, 41–67.

Nesterenko, V. (2001). *Dynamics of Heterogeneous Materials*. Shock Wave and High Pressure Phenomena. Springer-Verlag New York.

Ortiz, M., & Molinari, A. (1992). Effect of strain hardening and rate sensitivity on the dynamic growth of a void in a plastic material. *J. Appl. Mech.*, *114*, 48–53.

Sartori, C., Mercier, S., Jacques, N., & Molinari, A. (2015). Constitutive behavior of porous ductile materials accounting for micro-inertia and void shape. *Mech. Mater.*, *80*, 324–339.

Simo, J. C., & Hughes, T. J. R. (1998). *Computational inelasticity*. Interdisciplinary applied mathematics. New York, Berlin, Heidelberg: Springer.

Steinberg, D. J., Cochran, S. G., & Guinan, M. W. (1980). A constitutive model for metals applicable at highstrain rate. *J. Appl. Phys.*, *51*, 1498–1504.

Subramani, M., Czarnota, C., Mercier, S., & Molinari, A. (2020). Dynamic response of ductile materials containing cylindrical voids. *Int. J. Fract.*, *222*,197–218.

Swegle, J. W., & Grady, D. E. (1985). Shock viscosity and the prediction of shock wave rise times. *J. Appl. Phys.*, *58*, 692–701.

Taniguchi, S., & Ruggeri, T. (2018). On the sub-shock formation in extended thermodynamics. *Int. J. Non-Linear Mech.*, *99*, 69–78.

Tong, W., & Ravichandran, G. (1993). Dynamic pore collapse in viscoplastic material. *J. Appl. Phys.*, *74*, 2425–2435.

Tong, W., & Ravichandran, G. (1995). Inertial effects on void growth in porous viscoplastic materials. *J. Appl. Mech.*, *62*, 633–639.

Tvergaard, V. (1981). Influence of voids on shear bands instabilities under plane strain conditions. *Int. J. Fract.*, *17*, 389–407.

Versino, D., & Bronkhorst, C. (2018). A computationally efficient ductile damage model accounting for nucleation and micro-inertia at high triaxialities. *Comput. Methods Appl. Mech. Eng.* , *333*, 395–420.

Vogler, T. J., Borg, J. P., & Grady, D. E. (2012). On the scaling of steady structured waves in heterogeneous materials. *J. Appl. Phys.*, *112*.

Wang, Z. P. (1994). Growth of voids in porous ductile materials at high strain rate. *J. Appl. Phys.*, *76*, 1535–1542.

Wang, Z. P. (1997). Void-containing nonlinear materials subject to high-rate loading. *J. Appl. Phys.*, *81*, 7213–7227.

Wilkerson, J. (2017). On the micromechanics of void dynamics at extreme rates. *Int. J. Plast.*, *95*, 21–42.

Wilkerson, J., & Ramesh, K. (2014). A dynamic void growth model governed by dislocation kinetics. *J. Mech. Phys. Solids*, *70*, 262–280.

Wu, X. Y., Ramesh, K. T., & Wright, T. W. (2003a). The coupled effects of plastic strain gradient and thermal softening on the dynamic growth of a single void. *Int. J. Solids Struct.*, *40*, 6633–6651.

Wu, X. Y., Ramesh, K. T., & Wright, T. W. (2003b). The dynamic growth of a single void in a viscoplastic material under transient hydrostatic loading. *J. Mech. Phys. Solids*, *51*, 1–26.

Wu, X. Y., Ramesh, K. T., & Wright, T. W. (2003c). The effects of thermal softening and heat conduction on the dynamic growth of voids. *Int. J. Solids Struct.*, *40*, 4461–4478.

Xiang, M., Cui, J., Yang, Y., Liao, Y., Wang, K., Chen, Y., & Chen, J. (2017). Shock responses of nanoporous aluminum by molecular dynamics simulations. *Int. J. Plast.*, *97*, 24 – 45.

Zhuang, S., Ravichandran, G., & Grady, D. E. (2003). An experimental investigation of shock wave propagation in periodically layered composites. *J. Mech. Phys. Solids*, *51*, 245 – 265.

List of Figures

List of Tables